Development of Multimodal Imaging Probes Using Carbon Dots

Diego A. Mendoza

A Thesis

in

The Department

of

Chemistry and Biochemistry

Presented in Partial Fulfillment of the Requirements

For the Degree of Master of Science in Chemistry at

Concordia University

Montréal, Québec, Canada

January, 2023

CONCORDIA UNIVERSITY

SCHOOL OF GRADUATE STUDIES

This is to certify that the thesis prepared

By: Diego Mendoza

Entitled: Development of Multimodal Imaging Probes Using Carbon Dots

and submitted in partial fulfillment of the requirements for the degree of

Master of Science (Chemistry)

complies with the regulations of the University and meets the accepted standards with respect to originality and quality.

Signed by the final Examining Committee:

_____ Chair

Dr. Ashlee Howarth

_____ Examiner

Dr. Marek Majewski

_____ Examiner

Dr. John Capobianco

_____ Supervisor

Dr. Rafik Naccache

Approved by _____

Dr. Louis Cuccia, Graduate Program Director

January 12, 2023 _____

Dr. Pascale Sicotte, Dean of Faculty of Arts and Science

ABSTRACT

Development of Multimodal Imaging Probes Using Carbon Dots

Diego Mendoza

Molecular imaging techniques such as fluorescence and magnetic resonance imaging play a significant role in monitoring human health but individually, they possess limitations. To address their shortcomings, contrast agents are used to improve the quality of the images; however, concerns usually arise due to their toxicity. Carbon dots offer an interesting alternative to be developed as multimodal probes and offer contrast enhancement in imaging techniques owing to their versatile optical properties, simple preparation, and biocompatibility. Herein, the synthesis of dual-fluorescent carbon dots functionalized with Mn^{2+} is presented. The dots were prepared using L-glutathione and formamide in a microwave reactor resulting in concomitant blue and red optical signatures following excitation at 420 nm. Surface decoration with paramagnetic Mn^{2+} was investigated via two parallel approaches namely direct electrostatic interactions and through chelation with diethylenetriaminepentaacetic acid with subsequent coordination of the metal cation. We investigated the physicochemical and optical properties with focus on preserving the red fluorescence for optical imaging, while maximizing metal cation loading for the magnetic resonance imaging modality. *In vitro* magnetic resonance imaging studies allowed for the identification of a lead candidate that offers good performance with an evident enhancement of the contrast of images when compared to clinically available contrast agents. Furthermore, toxicity assays demonstrated the low cytotoxicity of the dots, as well as the ones modified with metal cations suggesting good biocompatibility of this probe. Our results suggest that these Mn^{2+}-doped carbon dots offer a strong potential as dual-modal contrast agents in fluorescence and magnetic resonance imaging applications.

Acknowledgements

First, I would like to express my deepest appreciation to my supervisor, Dr. Rafik Naccache, for giving the opportunity to come to Concordia and for his constant precious support and guidance through this project. I am also grateful for my committee members, Dr. Marek Majewski and Dr. Capobianco, for providing me with their insightful feedback. I would also like to acknowledge the lab technicians from Concordia, McGill, and UQAM for training me in different characterization techniques. Thanks should also go to collaborators at Universitdad del Rosario and Université Côte d'Azur, Dr. Alejandro Ondo and Dr. Béatrice Cambien, for involving me in one of their projects. Special thanks to Dr. Béatrice Cambien for hosting me in her lab in France and introducing me to the biology field and the French culture. I could also not have undertaken this journey without former and new members of the Naccache Lab and their unconditional help. Special thanks to Jun Ray for introducing me to this project and proving me with his priceless guidance. I would also like to extend my sincere thanks to the funding institutions that made this project possible. And lastly, I would like to say that I am deeply indebted to my family for their unconditional love through my whole life.

TABLE OF CONTENTS

List of Figures

List of Tables

List of Abbreviations

US	Ultrasound
CT	Computed Tomography
MR	Magnetic Resonance
PET	Positron Emission Tomography
SPECT	Single Photon Emission Computed Tomography
PL	Photoluminescence
FL	Fluorescence
P	Phosphorescence
CL	Chemiluminescence
BL	Bioluminescence
TL	Thermoluminescence
QY	Quantum Yield
IA	Imaging Agent
CCD	Charge-Coupled Device
NIR	Near-Infrared
SBR	Signal-to-Background Ratio
FDA	Food and Drug Administration
ICG	Indocyanine Green
MB	Methylene Blue
RF	Radiofrequency
CA	Contrast Agent
TE	Time Echo

TR	Time Repetition
SE	Spin Echo
GSE	Gradient Spin Echo
IR	Inversion Recovery
SPIO	Superparamagnetic Iron Oxide
USPIO	Ultrasmall Paramagnetic Iron Oxide
SPION	Superparamagnetic Iron Oxide Nanoparticles
CVD	Chemical Vapor Deposition
AFM	Atomic Force Microscopy
STM	Scanning Tunneling Microscopy
NRs	Nanorods
BBN	Bombesin
NPs	Nanoparticles
HA	Hyaluronic Acid
SD	Standard Diet
DIO	Diet Induced Obesity
HFD	High Fat Diet
TPA-T-TQ	4,4′-((6,7diphenyl[1,2,5]thiadiazolo[3,4-g]quinoxaline-4,9-diyl)bis-(thiophene-5,2-diyl))bis(N-(4-(tert-butyl)phenyl)-N-(p-tolyl)- aniline)
DSPE-PEG2000	1,2-distearoyl-sn-glycero-3-phosphoethanolamine-N[methoxy(polyethyleneglycol)-2000]
CNTs	Carbon Nanotubes
CDs	Carbon Dots

GQDs	Graphene Quantum Dots
CNDs	Carbon Nanodots
CQDs	Carbon Quantum Dots
CPDs	Carbonized Polymeric Dots
UV-Vis	Ultraviolet-Visible
UPCL	Up-Conversion Photoluminescence
PET	Photoinduced Electron Transfer
DOX	Doxorubicin
LEDs	Light-Emitting Devices
EDA	Ethylenediamine
FA	Folic Acid
BEV	Bevacizumab
Ce6	Chlorin e6
HA	Hyaluronic Acid
DTPA	Diethylenetriaminepentaacetic Acid
cDTPAA	Cyclic Diethylenetriaminepentaacetic Acid Anhydride
PBS	Phosphate Buffered Saline
EDC	-Ethyl-3-(3-dimethylaminopropyl) carbodiimide hydrochloride
MW	Molecular Weight
ICP-OES	Inductive Coupled Plasma-Optical Emission Spectroscopy
TEM	Transmission Electron Microscopy
PXRD	Powder X-ray Diffraction
ATR-FTIR	Attenuated Total Reflectance Fourier-Transform Infrared Spectroscopy

XPS	X-ray Photoelectron Spectroscopy
DMEM	Dulbecco's Modified Eagle Medium
FBS	Fetal Bovine Serum
NAA	Neutron Activation Analysis
ROS	Reactive Oxygen Species
PEI	Polyethyleneimine

1 Introduction

1.1 Molecular Imaging

Imaging allows for the formation of detailed images of specific sites inside the human body based on an interaction between different forms of radiation and tissues. Imaging is routinely used in clinical research to diagnose of a variety of diseases and monitor responses to therapies.[1] Anatomical imaging is the most conventionally used tool and relies on the study of conditions or ailments that a patient may experience and that could later be translated into a diagnosis. However, most diseases can only be observed when they are at their late stages and anatomic imaging techniques may fall short to detect these changes. Consequentially, the rate of success of treatments may decrease. In past years, molecular imaging has recently become a promising alternative gaining significant attention due to its ability to monitor biological processes and identify any structural, functional, or molecular abnormalities at the cellular and molecular level, thus leading to more rapid diagnosis while monitoring diseases in real time in a non-invasive approach.[2,3] For example, to diagnose cancer, anatomical imaging would provide information about the shape, size, and heterogeneity of a tumor that has already formed while molecular imaging would provide information about the potential formation of a tumor.[4] For this reason, advancements in the field of imaging play a critical role in detecting diseases in their early stages. Current molecular imaging modalities include fluorescence imaging, which exploits the light emission of fluorescent molecules and is very popular in cell imaging applications; ultrasound (US), which is dependent on high frequency waves and their resulting echo as they travel through different tissues; computed tomography (CT) which is based on the attenuation of X-rays caused by different tissues; magnetic

resonance (MR) imaging, a technique built upon the magnetic signal caused by the movement of the spin of the protons of water inside the body; and positron emission tomography (PET) and single photon emission computed tomography (SPECT), both of which are reliant on the emission of photons by a radionuclide that circulates through a tissue. The selection of the appropriate technique depends on multiple factors mainly including the spatial resolution and sensitivity required, the specific site of analysis, the depth of penetration, and the number of assessments required. Among these techniques, fluorescence and MR imaging offer a combination that provides numerous benefits and addresses multiple shortcomings especially since none of these two techniques require the use of ionizing radiation. Both techniques are described below in greater details in sections 1.2 and 1.3.[5–7]

1.2 Overview of Fluorescence Imaging

1.2.1 Photoluminescence

To better understand fluorescence imaging, it is necessary to introduce the concept of photoluminescence (PL). PL is the emission of light upon excitation of the electronic states of a susceptible molecule caused by the absorption of electromagnetic irradiation. This phenomenon can be manifested in different forms, depending on the excitation and relaxation mechanisms. For instance, it can be manifested as fluorescence (FL), characterized by the emission of photons which is triggered by an absorption of energy. Phosphorescence (P), another photoluminescent phenomenon, resembles the mechanism of fluorescence but the reemission of the absorbed energy will be released after a longer time. Moreover, it can also manifest as chemiluminescence (CL), where the emission of photons is triggered by a chemical reaction which by-products are electronically excited; bioluminescence (BL), which also results from a chemical reaction but in

this case within a living organism; thermoluminescence (TL), that relies on the emission of light after certain crystalline solids undergo heating; among others. For the purpose of this thesis, we will focus on FL.[8–13]

1.2.2 Electronic Transitions

Electrons of atoms and molecules are localized around the nucleus in a region of space called orbitals. Orbitals are arranged in electron shells with discrete energy values also known as energy levels where electrons are distributed. Upon excitation of an atom or molecule by irradiation, electronic transitions between energy levels can occur. These electronic transitions are driven by the intrinsic angular momentum of the electron which is described by the spin quantum number (m_s), and can take values of ±1/2. According to the Pauli's exclusion principle, electrons in an atom cannot have identical quantum numbers. Because of that, two electrons in a single atomic orbital or molecular orbital must have a different m_s. In other words, they must be oriented either in an antiparallel or spin paired configuration. This will result in the cancellation of their magnetic moments and the formation of a singlet state (S). Most molecules with an even number of electrons will form singlet ground states (S_0). When an electron is excited to a higher energy level, it can either maintain or change its configuration. In this sense, if it maintains its antiparallel orientation, an excited singlet state (S_x) is observed. On the other hand, if the electron changes its orientation to a parallel position relative to the original paired electron, a triplet state (T_x) will result (Figure 1).[14–17] The probable orientations of the spin angular momentum are dictated by the spin multiplicity and is expressed as 2S+1, where S represents the spin quantum number. Singlets are characterized by a multiplicity of 1 while triplets are characterized by a multiplicity of 3.[17]

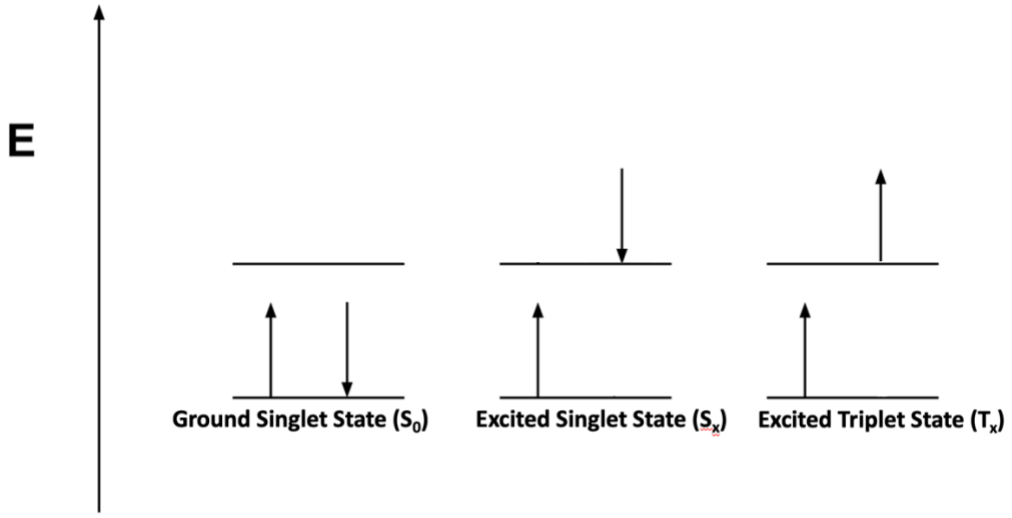

Figure 1. Schematic representation of singlet and triplet states.

According to quantum mechanics, the electronic transitions are limited by selection rules which determine whether they have a high probability of occurring or not. If an electronic transition has a high probability of occurring, it is referred to as an allowed transition. In contrast, if an electronic transition is less likely to occur, then it is referred to as a forbidden transition. The only allowed transitions are those who follow the rules which state that the orbital quantum number (l) of an electron changes by one ($\Delta l = \pm 1$) while its spin quantum number is maintained ($\Delta m_s = 0$) and which magnetic quantum number (m_l) either remains unchanged or changes by one ($\Delta m_l = 0, \pm 1$) otherwise the transition is considered forbidden. In this sense, transitions from T_x to the S_0 are forbidden while transitions from S_x to S_0 are allowed.[17,18]

1.2.3 Fluorescence

Fluorescence presents allowed transitions that originate from the absorption of a photon that promotes an electron from S_0 to an excited S_x state. This process is followed by the transition of

the electron from the lowest vibrational energy level of the excited S_x back to the original S_0 ground state, and the subsequent emission of a photon of a lower energy than the absorbed energy (Figure 2). Hence, fluorescence can be distinguished by the conservation of the spin multiplicity.[8] Both the excitation and relaxation processes are immediate, with a time range of femto- (10^{-15} s) and nanoseconds (10^{-9} s), respectively. The time a fluorescent molecule remains in the excited state is defined as fluorescence lifetime which depends on the nature of the fluorophore, and is affected by external factors including temperature, polarity, and the presence of fluorescence quenchers.[19,20]

On the other hand, relaxation can also occur in a non-radiative manner and is characterized by shorter lifetimes than those of PL. Given that electronic energy level is distributed in a substructure of a series of vibrational energy levels, transitions between levels occurs simultaneously resulting in FL. For instance, vibrational relaxation is observed when an excited molecule relaxes to the lowest vibrational level of the excited electronic state. Alternatively, internal conversion originates from an excitation to a higher lying level (S_x) with a higher energy than S_1 followed by a rapid relaxation to S_1. Conversely, intersystem crossing occurs between excited states of different multiplicity, namely from S_1 to T_1. Finally, non-radiative processes occur without the release of photons and often can be experimentally observed as a quenching of the PL. [21,22] With this in mind, it can be stated that both radiative and non-radiative process will take place during excitation and subsequent relaxation. The fluorescence efficiency of a molecule can be determined by the fluorescence quantum yield (QY), also represented as Φ_f, which is referred as the ratio of number of photons emitted to number of photons absorbed and takes into account all the de-excitation processes and is influenced by the number of energy levels. QY can be represented by the following equation:

$$\Phi f = \frac{k_f}{k_f + k_{nr} + k_t}$$

where k_f represents the rate constant of fluorescence, k_{nr} the rate constant of non-radiative decay, and k_t the rate constant of energy transfer. The value of the QY is dependent on the nature of the fluorophore and its electronic structure. [23,24]

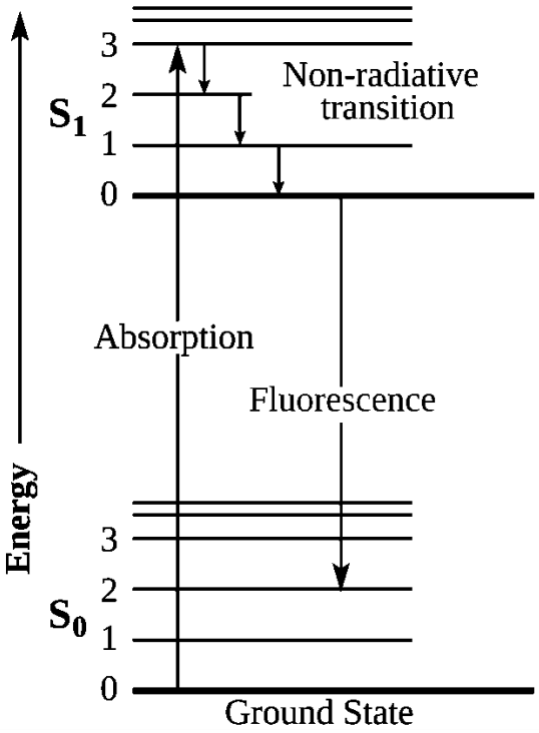

Figure 2. Simplified Jablonski diagram of fluorescence. A photon is absorbed exciting an electron from S_0 to S_x, followed by the transition of the electron to the S_0, resulting in the emission of a photon with a lower energy than the absorbed radiation.

Organic compounds with aromatic rings are the most notable molecules that undergo fluorescence.[24,25] The reason is that most of them are composed of a high-order π conjugation which translates into a small overlap among their π orbitals. Hence, reducing the band gap between the highest occupied molecular orbital and the lowest unoccupied molecular orbital.[26] The FL of molecules can be explored by irradiating a fluorophore with a range of wavelengths to produce a

spectrum of allowed transitions. The absorption and fluorescence spectra are characteristic of each fluorophore and can be exploited for characterization purposes.[22]

1.2.4 Fluorescence Imaging

Fluorescence imaging is a non-invasive and non-destructive technique that allows the visualization of cells and tissues in real time through the use of fluorescent molecules. In a typical fluorescence imaging analysis, a fluorescent imaging agent (IA) is first injected into a patient. Once inside the body, the IA is irradiated with light of a certain wavelength, depending on the type of probe. This will stimulate the emission of light from the fluorophore that has already accumulated in a specific site in the body. The emitted light signal will later be detected by a charge-coupled device (CCD) camera and then processed into images.[3] When compared to other molecular imaging techniques, fluorescence imaging offers lower costs, and higher sensitivity and specificity. Plus, the use of low-energy photons makes it safer than other techniques such as PET and SPECT.[27,28]

To illustrate fluorescence imaging, Figure 3 shows a series of images of human glioblastoma cells obtained by Macairan et al. by confocal microscopy where different cell organelles were labelled using a series of dyes. For instance, LysoTracker Green was used to label lysososmes, Tubulin Tracker Green for tubulin and MitoTracker Green for mitochondria. In addition, cells were also treated with carbon dots. The imaging process involved exciting the different dyes, and the nanoparticles, at different wavelengths taking advantage of their different emission wavelengths along the electromagnetic spectrum. As a result, it was possible to monitor the localization of the nanoparticles which most intense signals originated from the lysosomal compartments.[104]

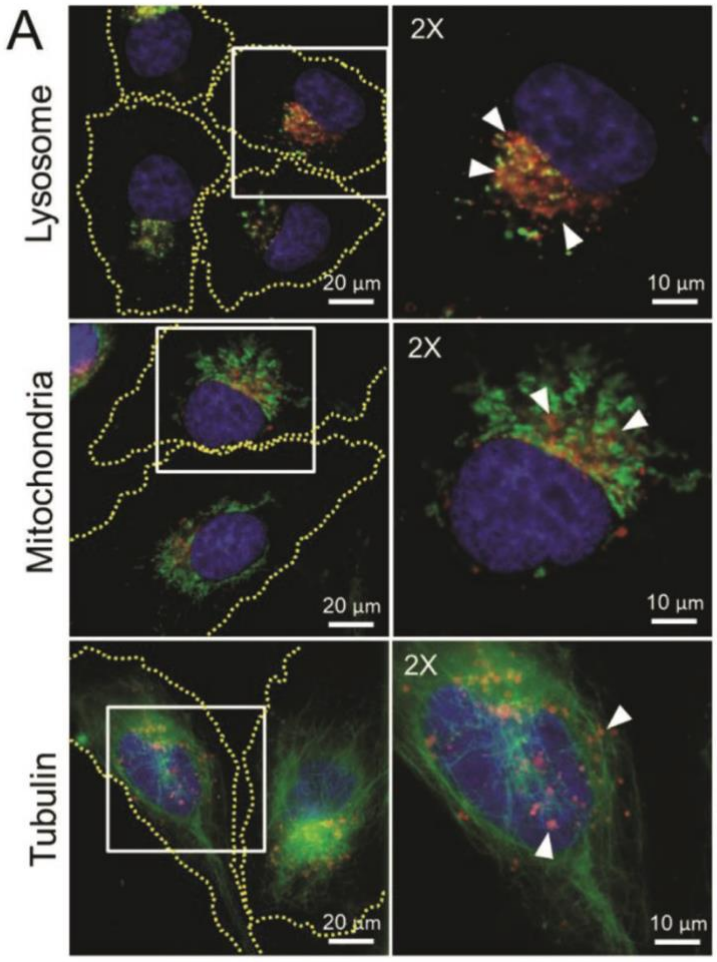

Figure 3. Intracellular localization of carbon dots (red) in cells colabeled for lysosomes, mitochondria, or tubulin. Reproduced with permission from "Ratiometric pH sensing in Living Cells Using Carbon Dots", by Macairan et al., 2020, *Particle and Particle Systems Characterization*. Copyright 2019 by WILEY-VCH Verlag GmbH & Co.[104]

But despite of its benefits, one of the main drawbacks of fluorescence imaging is associated with the scatter of photons at short wavelengths that is caused by tissues and cellular components, also known as autofluorescence. Nevertheless, the use of near-infrared (NIR) light (650 to 900 nm) for *in vivo* studies has been reflected as an approach towards background correction and improved tissue penetration. Below this region, usually cytochromes, hemoglobin, and water would take part in the attenuation and scatter of the signal. Also, the ability of low-energy photons to penetrate tissues is limited.[3] As a comparison, short wavelengths can hardly penetrate tissues in

the range of millimetres while longer wavelengths can penetrate a few centimeters. [29,30] Nevertheless, the use of specifically tailored imaging agents (IA) could help address these drawbacks.

1.2.5 Fluorescence Imaging Agents

As the previous example illustrated, molecular imaging techniques are usually accompanied by the use of IAs, whose main role is to improve the quality of the resulting images. IAs are mainly composed of a targeting and a signaling component. The signaling component depends on the type of technique being used, but some examples include radionuclides for SPECT, fluorophores for fluorescence imaging, and paramagnetic metals for MR imaging. On the other hand, the nature of the targeting component depends on where the probe will be localized. Small molecules, peptides, and antibodies are the most popular targeting components which are bound to the carrier structure. An ideal IA should offer affinity, selectivity, stability, multiplexing-ability, and low cytotoxicity. [3,31] Fluorescent IAs are known for their ability to emit light upon excitation, which facilitates the visualization of cellular processes.

Examples of fluorescent IAs include proteins, such as green fluorescent protein (GFP) which is extracted from the jellyfish *Aequorea Victoria* and is widely used to study protein interactions; chemical dyes, like fluorescein isothiocyanate which is commonly used in immunofluorescence and flow cytometry; and, more recently, nanoparticles, which will be later described.[30,32–34] To successfully improve the fluorescent signal and deal with autofluorescence, as well as the interference of biological components, ideal fluorophores should have emission wavelengths higher than 650 nm, namely in the NIR region. Nonetheless, at the moment, only two NIR fluorescent IAs that have been approved by the U.S. Food and Drug Administration (FDA)

are available: indocyanine green (ICG) and methylene blue (MB).[28] Other requirements for an efficient IA include improved quantum yield, wavelength-dependency, photostability, and biocompatibility.[35] Conventional IAs satisfy most of these characteristics, however, photobleaching has been a limiting factor in their use.[36] Photobleaching is the irreversible loss of the fluorescent properties of a fluorophore and is caused by a prolonged exposition to irradiation.[37] In this regard, low-intensity fluorescence signals lead to inaccurate results or offer limited sensitivity. To address the shortcomings of autofluorescence, tissue penetration, and photobleaching, nanomaterials have been explored and will be described in more detail in a later section.

1.3 Overview of Magnetic Resonance Imaging

1.3.1 Hydrogen Atom

The human body is primarily composed of tissues comprising water, fat, and proteins. These tissues are rich in hydrogen protons (^{1}H), which is the base of MR imaging. MR imaging is a technique that depends on the interaction between the spin of protons of a nucleus and an external magnetic field (B_0) to form images.[38] According to quantum mechanics, elementary particles such as electrons, neutrons and protons possess an intrinsic property named spin that will confer them an intrinsic angular momentum. From the classical mechanic point of view, the spin can be imagined as a physical sphere spinning around its own axis. Because of this movement, protons have the ability to produce a local B_0 and creating a dipole. Under normal circumstances, they are randomly distributed in space. When a strong external B_0 is applied, the nucleus will align either in the same direction or perpendicularly to the applied field, creating a magnetization vector.[39] During this interaction, protons will first begin to wobble, also known as precession, around the

axis of the B_0 field, and finally fall into a different plane. The frequency at which protons precess is also known as Larmor frequency and depends on the nature of the nuclei, the strength of the applied B_0, and the gyromagnetic ratio (γ).[38,40] The value of the Larmor frequency can be calculated with the following equation:

$$f = \gamma B_0$$

where f is the frequency of precession; γ is the gyromagnetic ratio, which is characteristic of each type of nuclei; and B_0 is the main magnetic field strength. In the case of hydrogen protons, the gyromagnetic ratio is 42.6 MHz·T^{-1}, resulting in a Larmor frequency of 64 MHz at 1.5 T.[38]

1.3.2 Relaxation

Relaxation can be described as the process by which a nuclear spin returns to thermal equilibrium after a radiofrequency (RF) excitation has been removed. Generally, relaxation processes can be classified into longitudinal and transversal, and they are identified by time constants T_1 and T_2, respectively.[39] The main difference is that T_1 characterizes the regrowth of the longitudinal magnetization while T_2 indicates the loss of the transverse magnetization.[41] In this sense, T_1 is the rate at which 63% of protons have recovered thermal equilibrium following a RF pulse. On the other hand, T_2 is the rate at which the transverse magnetization decays to 37 % of its original magnitude. In addition to T_2, T_2^* can also result from the loss of transversal magnetization, however, it will only surge in the case where the transverse magnetization dephasing occurs due to B_0 inhomogeneities and is not a useful indicator of a disease.[42] T_1 relaxation is driven by an exchange of energy between protons of water and protons attached to other molecules. By

convention, this is referred as spin-lattice relaxation time, where the surrounding nucleus environment is considered as the lattice. T_2 relaxation implies an exchange of energy among protons of water. As such, it is referred as spin-spin relaxation time. Both T_1 and T_2 are influenced by the random motion and interactions that have place in the biophysical and biochemical environment. Hence, T_1 and T_2 will vary depending on the nature of the tissue.[41]

1.3.3 Magnetic Resonance Imaging

The obtention of an image through MR imaging is a simple protocol based on nuclear magnetic resonance and the fact that hydrogen constitutes 80% of all atoms found in the human body. In a typical MR imaging protocol, an imaging agent, which has a main role to improve the contrast of the images, is administrated intravenously to the patient. Then, the patient is introduced in a chamber surrounded by cryogenic superconducting magnets that provide a field strength ranging between 0.5 and 1.5 T.[39] Once introduced in the chamber, a B_0 is applied and the randomly oriented protons of the body will align in the same direction of his field, also known the longitudinal or z direction. After, a 90° radiofrequency (RF) pulse at the Larmor frequency of ^1H protons is sent to the patient in a perpendicular direction to B_0 at the specific site that wants to be analysed. Because of the absorption of RF, ^1H protons are excited and will rotate into the transversal, or x-y direction, so the longitudinal direction will become zero. Once in the transversal plane, ^1H protons will start to precess in phase, resulting in the development of a net transversal magnetization. But because of spin-spin interactions, they will begin to dephase, or lose their phase coherence. Due to dephasing, the magnetic moments will cancel out, and the MR signal decreases. Completely dephased magnetization translates in the complete loss of the MR signal. After the RF is removed, ^1H protons will return to their original low-energy state releasing energy in the process. Both

relaxation processes happen simultaneously. The information about the energy released obtained from the recovery of the longitudinal net magnetization and the decay of the transversal magnetization can then be translated into images.[3,39,43,44] Figure 4 summarizes this process. The main advantage of MR imaging over other techniques is that it does not require the use of ionizing radiation, and it provides high spatial resolution and deep tissue penetration. Unfortunately, its main drawback is related to its poor sensitivity.[6,45,46]

The intensity of a B_0 is described in terms of tesla (T). Clinical MR imaging is typically conducted by using cryogenic superconducting magnets that provide a field strength ranging between 0.5 and 1.5 T. Now, stronger fields are used, for instance of 3 T, because of an improved signal-to-noise ratio (SNR) which contributes to reduce the imaging time. Some drawbacks are instability of the magnetic field, magnetic susceptibility, and other artifacts.[39] Nonetheless, low field MR imaging is still preferred because of a lower cost, more uniform magnetic fields, portability, and more sophisticated instrumentation that can achieve the same image quality of high-field MR imaging systems.[47]

1.3.4 T_1 and T_2 Weighted Images

To identify differences in contrast of tissues, both T_1 and T_2 can be exploited by the modification of some parameters including time echo (TE), time repetition (TR), and flip angle. Then it is possible to collect T_1 weighted images (T_1w), characterized by an accentuated T_1 signal, and T_2-weighted images (T_2w), with an enhanced T_2 signal. Tissues with short T_1 values (260 ms) produce bright images. Examples of materials that produce a hyperintense signal include fat, methemoglobin, melanin, proteinaceous fluid, paramagnetic metals, and chelated CAs. On the contrary, if a tissue has a long T_1 value (3000 to 5000 ms), they will appear dark. This is the case

of iron, water, air, bone, and collagen. Unlike in T_1w, some materials that produce bright signal in T_2-w images are fluid, edema, fat, and a few hemorrhagic products.[38,39,43,48,49]

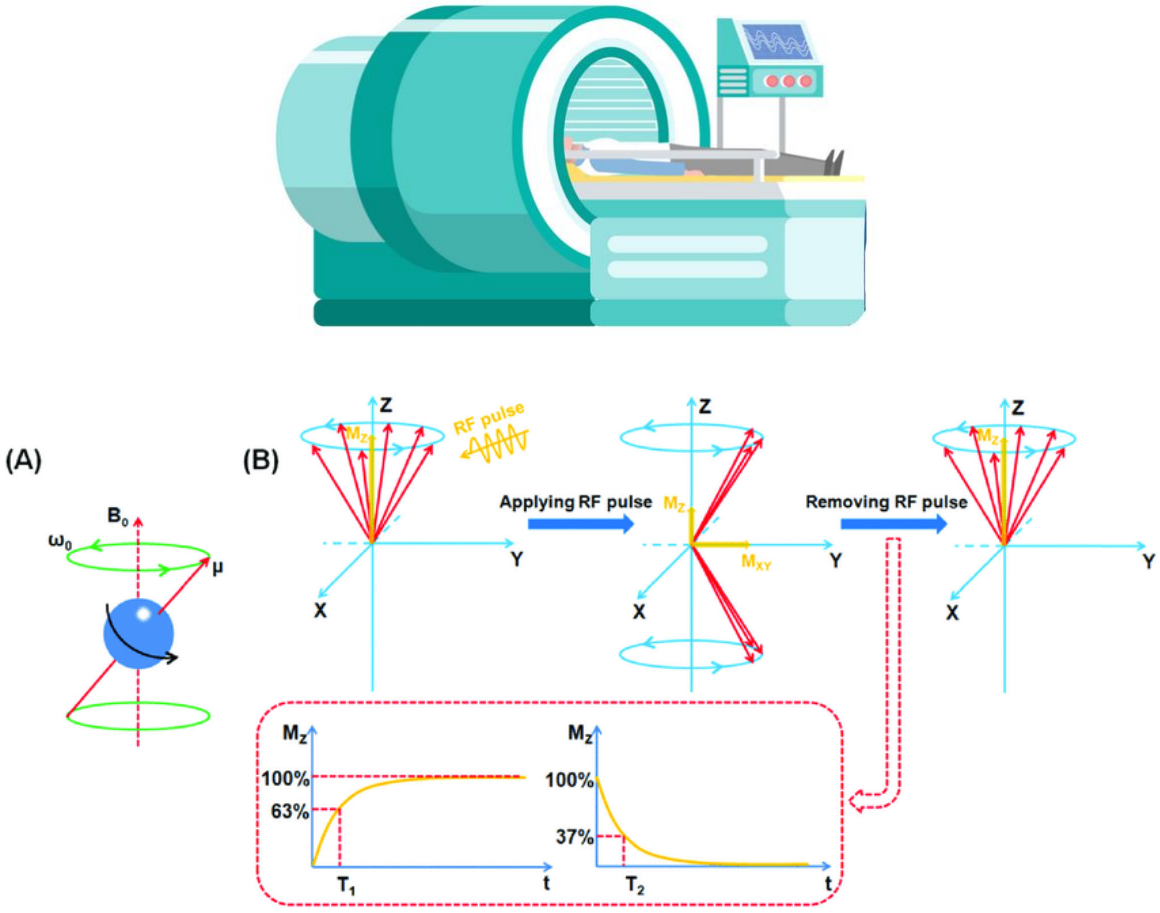

Figure 4. Schematic illustration of the mechanisms of MR imaging. a) Protons precess under external magnetic field B_0. b) After the introduction of RF pulse, protons are excited, with relaxation occurring following removal of the RF pulse. And the graphical representation of T_1 relaxation and T_2 relaxation. Reproduced with permission from "Gadolinium-based nanoscale MRI contrast agents for tumor imaging", by Cao et al., 2017, Journal of Materials Chemistry B, 5, 19. Copyright 2017 by Royal Society of Chemistry.[50]

1.3.5 Pulse Sequences

When the RF pulse causes the rotation of the net magnetization into the transverse plane x-y, it is considered as a 90° RF pulse. When the magnetization rotates into the opposite direction of the z-plane, we talk about a 180° pulse. A pulse sequence is a specific setting of the parameters in order

to produce the desired contrast in MR images. The most common pulse sequences can be classified into spin echo (SE), gradient spin echo (GSE), and inversion recovery (IR). Though, the variety of pulse sequences is extensive and most of them are simple variations of these three types.[39,48,51]

1.3.6 Spin Echo

Following a 90° RF pulse, protons will rotate into the transversal plane and start to dephase. Nonetheless, if a 180° pulse is applied, the spin will rotate to the opposite x-y direction. As a consequence, they will begin to rephase rather than dephase. If this 180° RF is applied once again, it will result in the same effect. The rephasing of the spin is termed echo. In that regard, TE is the time between the highest signal produced by the 90° RF pulse and the highest signal of the echo. TR, on the other hand, is defined as the time between successive pulse sequences. With typical values of TE and TR (at 1.5 T) of 20 and 500 ms, and 80 and 2000 ms, both T_1w and T_2w images can be obtained, respectively.[39,49]

1.3.7 Gradient Recalled Echo

In this case, the initial pulse is smaller than 90°. This will result in a shorter TR, so GRE is typically used to generate images in a faster manner. Plus, there is no 180° RF pulse applied, so only T_1w and T_2*w images can be obtained.[38,39]

1.3.8 Inversion Recovery

The IR pulse sequence is typically used to supress any unwanted signals. More predominantly, the fat signal. If a 180° is firstly applied, the longitudinal magnetization will rotate in an antiparallel z direction. Correspondingly, the magnetization will regrow in the original direction. Once at the

zero axis, a 90 ° RF is applied, eliminating the signal. Hence, resulting in a dark image. The time inversion (TI), which is the time between the 180° RF and the 90° RF pulse, provides information to construct the image. Typical TI values to supress the fat signal are 170 ms (at 1.5 T), which typically results in T_2w images.[39,49]

1.3.9 Magnetic Contrast Agents

Magnetic resonance imaging agents, also known as CAs, are characterized by their magnetic properties that accelerate the relaxation process of neighbouring protons when exposed to a magnetic field. As a result, they can enhance the contrast difference between normal and abnormal tissues in which they are distributed, which results in brighter images. Figure 5 illustrates this effect in the comparison between two T_1 images taken from the same region of the brain before and after administration of a CA highlighting the structure of a tumor. CAs are typically administrated intravenously in an MR imaging study. In general, they can be classified depending on their magnetic properties as positive or negative. Positive CAs increase the T_1-weighted signal by shortening T_1 of neighbouring water protons. On the other hand, negative CAs decrease the T_2-weighted signal by shortening T_2. Typically, positive CAs are composed of small molecular weight paramagnetic ion complexes, clinically available agents include Gd (III)-DTPA), Gd(III)-DOTA, Gd(III)-DO3A, and Mn(II)-DPPP. Meanwhile, negative CAs comprise more novel probes which are based on superparamagnetic materials such as superparamagnetic iron oxide (SPIO) and ultrasmall paramagnetic iron oxide (USPIO), which also have been commercialized. In spite of that, the only nanoparticle-based MR CA that has been approved by the FDA is composed of superparamagnetic iron oxide nanoparticles (SPIONs), and is suitable for T_2 and T_2*-weighted images.[3,52,53]

The majority of CAs are based on Gd^{3+} owing to its stability, long electronic spin relaxation time, and superior magnetic moment due to its 7 unpaired electrons in its 4f orbitals. When Gd^{3+} ions are in the proximity of protons of water, they will form a complex and reduce their relaxation time. As a result, images with enhanced quality are obtained.[54] Gd^{3+} then can shorten the T_1-weighted signal at low concentrations. However, high concentrations have proven to shorten the T_2-weighted signal instead. While both T_1 and T_2-weighted images are useful to identify abnormalities in tissues, positive CAs are preferred in conventional clinical practice to prevent the potential cytotoxic effects of metal ions. [53] Plus, Gd-based CAs can provide only a limited contrast enhancement, with r_1 values ranging between 3 and 4 $mM^{-1}{\cdot}s^{-1,}$ at 0.47 T, and which decreases as the magnetic field strength is increased.[55] The risk associated with the use of Gd^{3+} is predominately associated with the similarity in ionic radius with Ca^{2+}. When Gd^{3+} is introduced in the body in its free form, Gd^{3+} will bind to Ca^{2+} ion channels and to proteins that normally bind to Ca^{2+}. This effect is also known as transmetallation.[51]

But even though the cytotoxicity risks have been successfully addressed by developing probes where metal ions are chelated instead of the free metal, in 2007, the use of Gd^{3+}-based CAs was associated with the diagnosis of nephrogenic systemic fibrosis (NSF), specifically in patients with kidney disorders. As a response, the U.S. FDA released in 2010 a series of guidelines to avoid the use of Gd-based CAs in some patients. More recently, in 2017, these guidelines were updated after finding that Gd^{3+} can be retained in the body for a long term. This was then followed by the suspension of some CAs in Europe in 2018.[56,57] Now, the research community continues making efforts towards developing safer and more efficient probes.

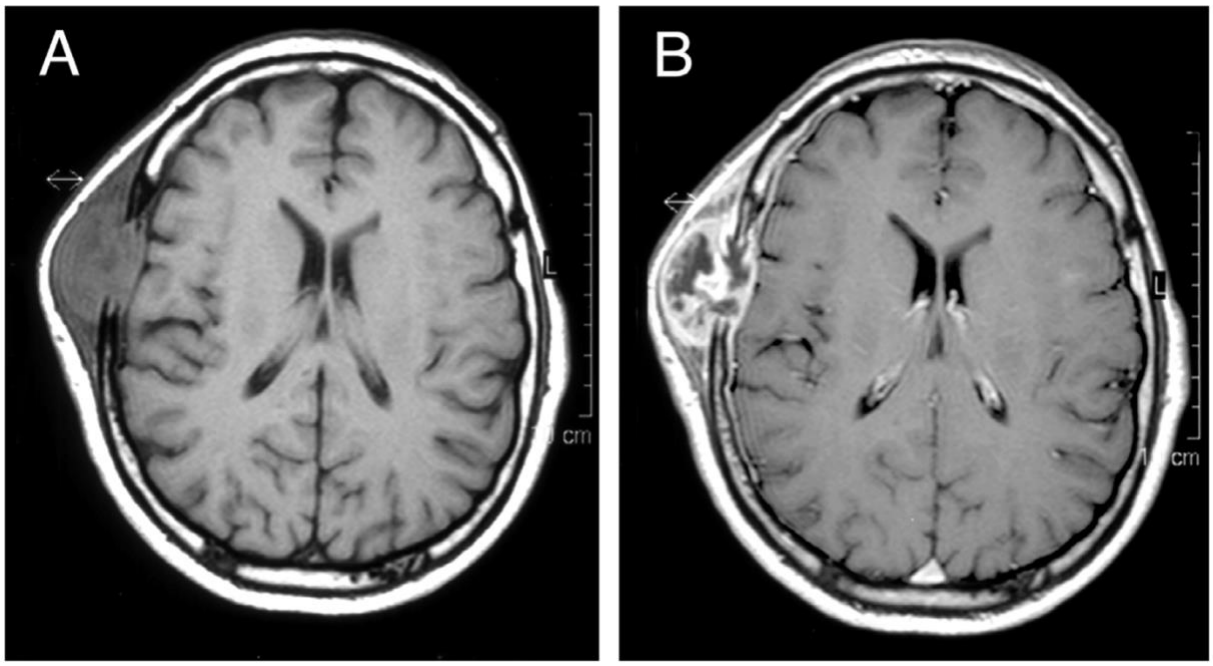

Figure 5. T_1 weighted MR image of brain (a) before, and (b) after Gadolinium contrast enhancement showing a metastatic deposit involving the right frontal bone with a large extracranial soft tissue component and meningeal invasion. Reproduced with permission from "Trauma-Associated Growth of Suspected Dormant Micrometastasis", by El Saghir et al., 2005, BMC Cancer, 5, 94. Copyright 2005 by El Saghir et al; license: https://creativecommons.org/licenses/by/4.0/legalcode. [58]

1.3.10 Relaxivity

Relaxivity can be defined as the degree to which a CA enhances the longitudinal or transverse relaxation rates (R_1, or $T_1^{-1,}$ and R_2, or T_2^{-1}, respectively) as a function of the concentration of the CA. For instance, higher relaxivities are associated to a higher shortening of the relaxation time, hence increasing the intensity of the produced signal. Relaxivity is characterized by r_1 and r_2 which represent the longitudinal and transversal relaxivity, respectively, and depends on the temperature, the field strength, and the type of substance in which the CA is dispersed. r_1 and r_2 values are typically obtained from the slope of the resulting plot of relaxation rates versus concentration of CA. Higher relaxivities are associated with the use of lower doses to provide a similar contrast

than high doses of compounds with low relaxivities. Thus, the development of CAs with high relaxivities will contribute to reduce the risk of metal-induced cytotoxicity.[59–61]

1.4 Nanomaterials

Nanomaterials are generally defined as materials with at least one dimension with a size of less than 100 nm. At the nanoscale, the properties of matter are distinct when compared to their bulk counterparts. Fundamentally, nanomaterials are unique owing to their properties, which differ from bulk including surface area, magnetism, quantum effects, conductivity, mechanical, catalytic, and in some cases antimicrobial properties: They can be obtained through two different approaches: top-down and bottom-up. Bottom-up approaches rely on building nanostructures from the self-assembly of atoms and molecules, also considered as building blocks, while top-down approaches focus on fabricating nanostructures from bulk materials. Some bottom-up techniques include chemical vapor deposition (CVD),[62] solvothermal,[63] hydrothermal,[64] sonochemical,[65] reverse micelle,[66] and exfoliation.[67] Top-down techniques include mechanical milling,[68] laser ablation,[69] arc discharge,[70] and photolithography.[71] During the past decade, numerous types of nanomaterials have been developed and applied in a wide range of fields. In a general picture, nanomaterials can be classified because of their chemical composition into carbon based, nanoporous, semiconductor, metal-based, and composites (Figure 6). And their applications have found place in cosmetics, semiconductors, sensors, catalysis, agriculture, good packaging, environmental remediation, construction, medicine, etcetera. Consequently, novel materials have emerged with enhanced features that outperform conventional materials. In the literature, there are several review articles available that describe nanomaterials in depth.[72–76]

When compared to conventional IAs, nanomaterials offer unique optical properties with superior photostability, longer circulation times, the possibility to attach targeting molecules and use them as drug delivery vehicles with high affinity, and multifunctionality. Potentially, they can contribute not only to diagnostics but also to therapeutics, a concept known as theranostics. For instance, to demonstrate the capability of nanomaterials in the molecular imaging field, Chanda et al. bioconjugated gold nanorods with bombesin (AuNRs-BBN), a 14-aminoacid peptide, to image tumor cells. The interaction of AuNRs-BBN with human prostate cancer (PC-3) and breast cancer cell lines (T-47D) was tested via dark field optical microscopy. The *in vitro* performance of AuNRs-BBN demonstrated high affinity towards both types of cancer cells. The advantages of using gold nanoparticles (AuNPs) over conventional fluorescent dyes, is their resistance to photobleaching. Plus, multiplexed approaches can also be implemented by using AuNPs of different sizes and shapes.[77,78] In another example, Rho et al. synthesized self-assembled hyaluronic acid NPs (HA-NPs) for targeted imaging. After administration into lean mice that were fed a standard diet (SD), and diet-induced obesity (DIO) mice fed a high fat diet (HFD), the probes were monitored with NIR fluorescence, showing strong signals in the liver and kidney attributed to the uptake by the reticuloendothelial system. HA-NPs were further tested in DIO mice, showing that HA-NPs supressed adipose tissue inflammation by reducing the macrophage content, inhibiting the production of proinflammatory cytokines and NLRP3 inflammasome activity. Interestingly, an empty HA-NP not bearing any drug showed these therapeutic effects.[79] In another work, Qi et al. synthesized NPs by encapsulating 4,4′-((6,7diphenyl[1,2,5]thiadiazolo[3,4-g]quinoxaline-4,9-diyl) bis-(thiophene-5,2-diyl))bis(N-(4-(tert-butyl)phenyl)-N-(p-tolyl)- aniline) (TPA-T-TQ) with 1,2-distearoyl-sn-glycero-3-phosphoethanolamine-N-[methoxy-(polyethyleneglycol)-2000](DSPE-PEG2000), an amphiphilic biocompatible copolymer, to

develop a supramolecular probe with intense absorption in the NIR region. Photothermal studies *in vivo* of TPA-T-TQ NPs using an 808 nm laser triggered an increase of the temperature that caused inhibition of tumor growth with no signs of side toxicity. Plus, TPA-T-TQ NPs were highly resistant to photobleaching and reactive oxygen species.[80] These examples demonstrate that different types of simple and complex nanomaterials have been developed as promising alternatives that could outperform conventional imaging agents.

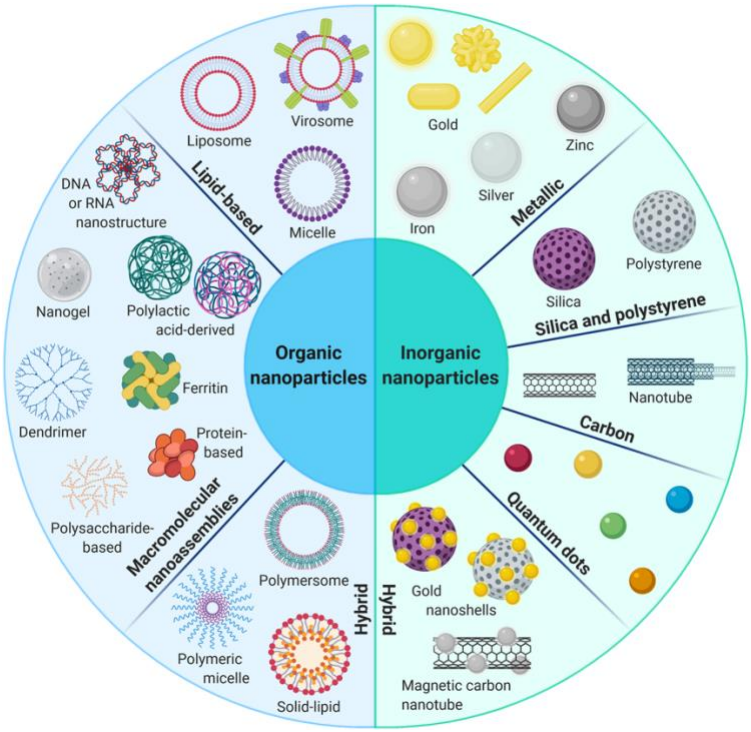

Figure 6. Nanomaterials in theranostics. Reproduced with permission from "Delivery of Cancer Therapies by Synthetic and Bio-Inspired Nanovectors", by Briolay et al., 2021, Molecular Cancer, 20, 55. Copyright 2021 by Briolay et al., license: license: https://creativecommons.org/licenses/by/4.0/legalcode.[81]

1.4.1 Carbon-Based Nanomaterials

Carbon-based nanomaterials include carbon nanotubes (CNTs), fullerenes, graphene, nanodiamonds, and carbon dots (CDs).[76] They have interesting properties such as high mechanical

strength, high conductivity and bright photoluminescence, among others. Despite being predominantly composed of the same atoms, carbon-based nanomaterials can differentiate primarily by their structure. Graphene, for example, is composed of a monoplanar sheet of sp^2-bonded carbon atoms in a hexagonal arrangement; CNTs are based on a single graphene layer arranged in a cylindrical shape; fullerenes are formed entirely of carbon atoms in a spherical, ellipsoidal, or tubular arrangements; nanodiamonds are nanocrystals of tetrahedrally bonded carbon atoms arranged in a 3D cubic lattice; and CDs are clusters of carbon with other atoms such as oxygen and hydrogen.[82–85] This thesis will focus on CDs as they are central to the development of the dual modal imaging probes reported in the coming chapters.

1.4.1.1 Carbon Dots

CDs are defined as zerodimensional quasispherical carbon-based materials that are less than 10 nm in size (Figure 7). They were discovered by accident in 2004 by Xu et al. during the electrophoretic purification of single walled carbon nanotubes.[86] Since their discovery, they have attracted significant attention because of their unique properties including tunable photoluminescence, photostability, chemical stability, and low cytotoxicity. These properties are predominantly influenced by the functional groups attached to the surface, including amine, carboxyl, and hydroxyl groups. Plus, CDs can be obtained from a wide range of low-cost and readily available precursors using a multitude of synthesis approaches such as one-step microwave or hydrothermal methods, which comprise more facile, affordable, and environmentally friendly synthetic procedures when compared to other nanomaterials. For these reasons, they have been explored in various fields such as catalysis, sensing, drug delivery and bioimaging.[87–96]

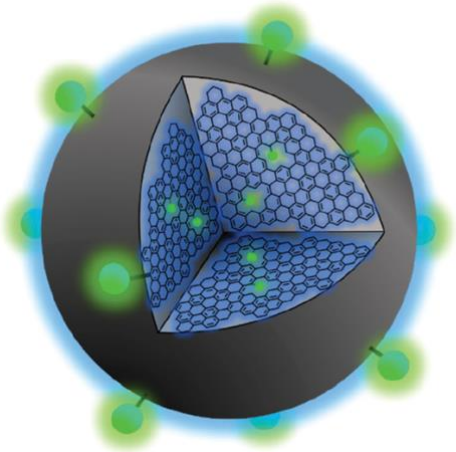

Figure 7. Schematic representation of a carbon dot.

1.4.1.2 Classification of Carbon Dots

Carbon-based nanodots are broadly divided into three categories: graphene quantum dots (GQDs); carbon nanodots (CNDs), or carbon quantum dots (CQDs); and carbonized polymeric dots (CPDs) (Figure 8)._ GQDs, are characterized by their graphene single or multilayer with functional groups at the surface. Their optical properties are driven by the size of π-conjugated domains and the surface structures. CQDs, are distinguished by their spherical multi-layer graphite core with functional groups in their surface. Their optical properties depend on the quantum confinement effect, or on core and surface states. CPDs, consist of aggregated or cross-linked carbon cores and polymer chain shells. Their optical properties are determined by their molecular state and cross-link structure.[96–98] This research focuses on CQDs, also simply termed CDs.

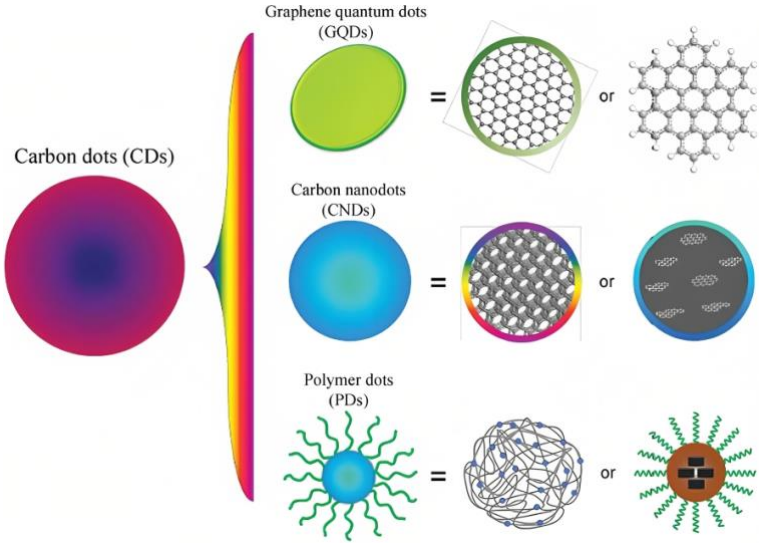

Figure 8. Classification of CDs. Reproduced with permission from "Advances in Fluorescent Carbon Dots for Biomedical Applications", by Koutsogiannis et al., 2020, Advances in Physics, 5, 1. Copyright 2021 by Koutsogiannis et al., licence license: https://creativecommons.org/licenses/by/4.0/legalcode. [99]

1.4.1.3 Synthesis of Carbon Dots

As most nanomaterials, CDs can be either prepared through top-down or bottom-up approaches. Top-down approaches offer simple operation and large-scale production. One such example is chemical exfoliation where the carbon sources are cleaved by strong acids or oxidizing agents. Another is laser ablation that is based on breaking down the precursors into nanoparticles *via* a high-intensity laser treatment. Lastly, ultrasonic-assisted treatments rely on hydrodynamic shear forces derived from the collapse of small bubbles in a solvent to break the macroscale precursors.[96,97]

On the other hand, most bottom-up techniques offer advantages of low costs, short reaction times, CDs with higher quantum yields, the use simple instrumentation, the possibility to carry out solvent-free reactions, the potential to scale up, and more control over reactions. By controlling the reaction parameters like time, pressure, and temperature, the properties of CDs can be tuned.

Bearing that in mind, bottom-up approaches are preferred over top-down to synthesize CDs. For instance, microwave synthesis is grounded on proving uniform heating through microwave irradiation to trigger the reaction to produce nanoparticles. Hydrothermal synthesis generally results in the obtention of unique properties and morphologies due to water being used as the only solvent. In this technique, a water solution of mixture is enclosed with Teflon, placed in an oven, and the mixture reaches high pressure and temperature conditions to trigger the reaction. Solvothermal synthesis is based on the same principle of hydrothermal synthesis with the exception that water is replaced by other solvents. Pyrolysis, another technique, utilizes high temperatures to heat, dehydrate, degrade, and finally carbonize organic materials. During this process, high concentration acids or bases are used to cleave the precursors into nanoparticles. Lastly, through chemical carbon deposition, volatile precursors are condensed into a chamber and deposited onto a surface.[96,97]

1.4.1.4 Properties of Carbon Dots

Properties of CDs depend highly on the synthetic route and the precursors. Despite this, they share common properties that are attractive for molecular imaging.[97] Due to their surface groups, CDs can absorb light at different regions of the ultraviolet-visible (UV-Vis) spectrum. The presence of sp^2 conjugated carbon translates to π-π^* transitions, while hybridization with heteroatoms will result in n-π^* transitions.[100]

Undoubtedly, the ability to emit light is one of the most appealing features of CDs that has characterized them over the years. Some of their FL properties include excitation wavelength-dependent emission, tunable emission, and resistance to photobleaching. The origin of their FL is still a matter of debate and some researchers have been trying to elucidate the mechanism behind

it, suggesting that fluorescence of CDs can result from a combination of mechanisms rather than just one.[101] However, there are two models that have been widely accepted. The first approach suggests that electronic transitions in the highly conjugated π- domains are responsible for the FL. This is also known as the quantum confinement effect, where the band gaps decrease as aromatic rings increase (e.g. increase in π conjugation), that in turn depends on the particle size. Normally, small nanoparticles emit at short wavelengths while large nanoparticles emit at long wavelengths. Thus, by controlling the size of CDs, their FL properties can be adjusted. The second approach is based on the idea that surface defects and/or surface functional groups, are what cause the FL. It has been established that heteroatoms modify the electronic structures of CDs by the addition of energy levels, that in turn results in an array of emissive traps. Increasing the number of surface functional groups will then result in more surface defects which will further result in red-shifted emissions.[96–98,100–102]

Besides FL, CDs possess up-conversion photoluminescence (UPCL) properties. Up-conversion is observed when two or more photons are simultaneously absorbed resulting in the emission of light at a shorter wavelength that promoted the excitation. This might be relevant for NIR fluorescence imaging. Unfortunately, new findings suggest that CDs might not provide a significant UCPL.[97,102] In addition, CDs have shown a photoinduced electron transfer (PET) property. In other words, they can act as an electron acceptor, as well as an electron donor. Because of this, in the presence of electron acceptors or electron donors, the PL from CDs is quenched.[96] This unique feature has been previously exploited to sense metals, as well as measure pH and temperature in cells by following a ratiometric approach speaking to their potential in fluorescence imaging applications.[103–105] In addition, owing to their nature, CDs have shown low and sometimes negligible cytotoxicity when evaluated both *in vitro* and *in vivo*. Moreover, because of the

hydroxyl-containing groups on their surface, CDs are highly dispersible in water so they can easily circulate through the vascularly system. Moreover, due to their sizes, they can be effortlessly uptaken by cells or penetrate the blood brain barrier (BBB).[106,107]

1.4.1.5 Carbon Dots in Molecular Imaging Applications

Because of to their low cytotoxicity, fluorescence QYs, resistance to photobleaching and tunable optical properties, CDs hold a great potential as fluorescent probes for *in vivo* imaging. Since they show an excitation-dependent multicolor emission, they provide versatility, which will avoid the need of using multiple probes. Plus, their surfaces can be modified with different types of moieties to target specific sites, or even to add functionalities.[97,108–110] As an example, Naik et al. recently synthesized nitrogen doped CDs (N-CDs) via hydrothermal synthesis for the detection of dopamine. The interaction of N-CDs with a series of biomolecules (such as L-tyrosine, citric acid, dopamine) was tested *in vitro* via fluorescence response resulting in a highly selective qualitative quantification of dopamine in a commercial pharmaceutical sample with a range for detection of 2 to 20 $\mu g \cdot mL^{-1}$ and a detection limit of 1.97 $\mu g \cdot mL^{-1}$. Because the interaction of dopamine with N-CDs quenched their fluorescence, the intensity of color changed as function of the concentration of dopamine. Then, by incorporating N-CDs in gel strips, it was possible to achieve a naked-eye detection approach. [111] Moreover, Geng et al. prepared mitochondria-tracking CDs (MitoCDs) consisting of a rhodamine structure trough retrosynthesis using citric acid, which contains multiple carboxyl and hydroxyl groups, and m-aminophenol. Resulting green to red fluorescent MitoCDs with QYs as high as 0.40 % were successfully used for mitochondrial targeting imaging of HeLa cells *in vitro*. Interestingly, the probes remained trackable for as long as six passages which is beneficial for long-term cell imaging. The lipophilic cationic dye rodamine center allowed the

researchers to monitor changes in the mitochondrial internal environment. MitoCDs were highly phostable with a remaining 90% fluorescence intensity after 1 h of irradiation.[112] Furthermore, Wu et al. constructed a CD-based theranostic nanoplatform for imaging and gene delivery. CDs were first multifunctionalized to produce targeted folate-conjugated reducible polyethyleneimine passivated CDs (fc-rPEI-CDs). Multiple siRNAs (EGFR and cyclin B1) were encapsulated (fc-rPEI-CDs/pooled siRNA) for its further release to treat lung cancer. fc-rPEI-CDs/pooled siRNA were monitored both *in vivo* and *in vitro* through bioluminescent imaging owing to their blue photoluminescence at 360 nm excitation. The improved anticancer effect was attributed to the ability of fc-rPEI-CDs/pooled siRNA to selectively bind receptor mediated endocytosis. It is noteworthy to mention that the viability of human lung cancer (H460) cell line demonstrated low cytotoxicity with more than 70% remaining alive after 3 days of treatment with fc-rPEI-CDs/pooled siRNA.[113] Other works have reported the use of N-CDs as label-free probes for the intracellular detection of silver ions and glutathione, red emitting p-phenylenediamine CDs (pPCDs) for nucleolus-targeteded imaging, dual-emissive N,S co-doped CDs (N, S-CDs) with reversible fluorescence for simoultaneous pH sensing and imaging, among others.[95,114–116]

Thus, the most remarkable contribution of CDs in molecular imaging, is their ability to provide an enhanced effect at low efficient doses. Moreover, unlike bulk materials, CDs have the ability to circulate the body without interfering with the blood flow, and because of their sizes they can potentially penetrate biological barriers and avoid being eluded by the reticuloendothelial system.[117]

1.4.1.6 Carbon Dots-Based Multimodal Probes as a New Approach in Molecular Imaging

Current challenges in the molecular imaging field involve developing more sophisticated probes with high quantum yields, high stability, and low cytotoxicity. During the past few years, efforts have been made to develop probes with the novel approach of tailoring CDs with additional properties to adapt them for two or more molecular imaging modalities.[46,118] For instance, MR imaging offers high spatial resolution and deep tissue penetration, but it lacks in sensitivity. Fluorescence imaging, on the other hand, provides high sensitivity. Given this complementarity between modalities, fluorescent CDs have been adapted with paramagnetic ions, resulting in magnetofluorescent probes with high quantum yields, and enhanced relaxivities.

One of the first approaches towards developing multimodal probes was reported by Shi et al. In their work, they synthesized luminescent CDs from citric acid, and polyethyleneimine (PEI) followed by the conjugation of DTPA and the further chelation of Gd^{3+} ions onto the surface of CDs. DTPA is a synthetic chelating agent composed of an aminopolycarboxylic acid with diethylene triamine backbone and five carboxymethyl groups and is known to form soluble stable complexes with different heavy metal ions including Cu(II), Ni(II), Co(II), Zn(II), Cd(II), Mn(II) and Ca(II), at an equimolar ratio over a pH range of 3 to 11.[119] The conjugation of DTPA to the surface of CDs can be achieved by the one-step water-soluble carbodiimide mediated strategy which involves the use of carboxyl-reactive chemical groups also known as carbodiimide crosslinkers. Most popular carbodiimide compounds are 1-ethyl-3-(-3-dimethylaminopropyl) carbodiimide hydrochloride (EDC) and N', N'-dicyclohexyl carbodiimide (DCC), whose main role is to crosslink carboxylic acids to primary amines. They are used in carbonyl group activation due to the resistance to H_2O resulting from the amide bond production, leading to higher reaction

yields.[120] According to their protocol, DTPA is converted into its cyclic anhydride form (cDTPAA) (Figure 9) to make carboxyl groups available for a coupling reaction.

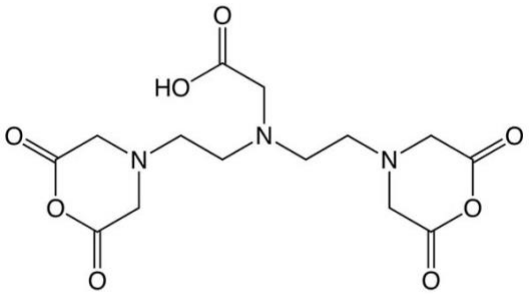

Figure 9. Structure of cyclic diethylenetriaminepentaacetic acid anhydride (cDTPAA).

Then, cDTPAA is conjugated onto the surface of CDs with the help of EDC. An overview of this reaction is depicted in Figure 10. Fundamentally, EDC will react with the carboxyl groups of cDTPAA to produce an unstable active O-acylisourea intermediate. Subsequently, the primary amines on the surface of CDs form an amide bond with the cDTPAA carboxyl groups while an isourea by-product is released.[120] The final product of the reaction are the Gd-doped CDs. The resulting Gd-doped CDs demonstrated FL/MR capabilities, providing a bright blue photoluminescence at an excitation wavelength of 460 nm with a quantum yield (QY) of 5.2% and a significantly high r_1 value of 56.72 $mM^{-1}s^{-1}$. Hence surpassing the efficiency of conventional dyes.[121]

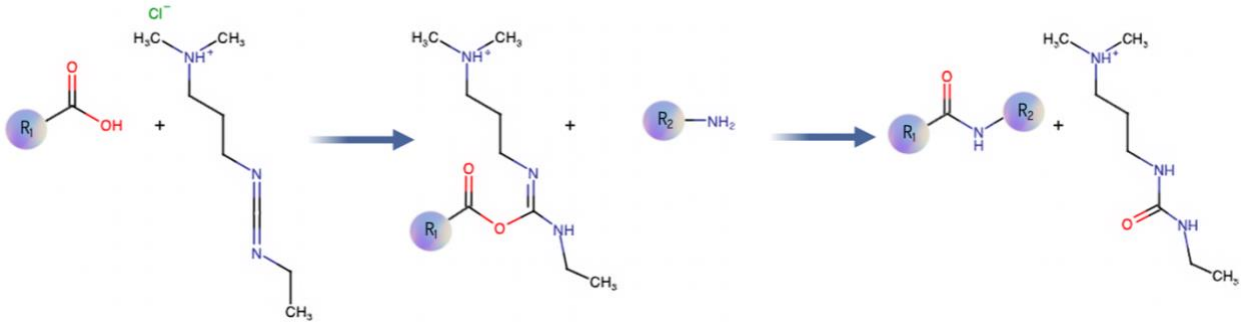

Figure 10. Scheme of crosslinking reaction between carboxyl and amine groups to form an amide bond driven by carbodiimide chemistry.

In a more recent work, Zheng et al. prepared Gd-doped CDs from L-arginine that was able to reach the kidneys in mice after 30 minutes of being administered with a low reported long-term cytotoxicity. The QY and r_1 reported were 57.8%, and 6.27 $mM^{-1}s^{-1}$, respectively.[122] Similarly, Maghsoudinia et al. obtained Gd-doped CDs using citric acid, Gadovist (Gd-DO3A-butrol) and ethylenediamine (EDA). Gd-doped CDs were further functionalized with both folic acid (FA) and bevacizumab (BEV), resulting in a QY of 83.7%, and tested both *in vitro* and *in vivo* to target hepatocellular carcinoma. Internalization into Hepa1-6 cells and improvement of MR contrast, with the highest r_1 being 7.98 $mM^{-1}s^{-1}$, were achieved.[5] Other works have demonstrated comparable results.[123,124]

But despite the superior relaxivities that Gd-loaded CDs can offer, their potential cytotoxicity remains a concern. As a response, other authors have proposed the use of Mn^{2+} due to its magnetic properties (resembling those of Gd^{3+}) with its five unpaired electrons. Hence, it can offer a high spin number and long electronic relaxation times. Unlike Gd^{3+}, Mn^{2+} can be naturally found in mitochondria-rich organs and is used as a cofactor for some enzymes and receptors.[125] To date only two Mn-based CAs are clinically available, Teslascan (Mn-DPDP) and Lumenhance (containing $MnCl_2$). However, Mn-DPDP, or the chelated form, has a low longitudinal relaxivity

of 1.88 $mM^{-1}s^{-1}$ at 37 °C. On the other hand, the CAs containing $MnCl_2$ can be toxic since metals are free in a free form.[44]

Within this framework, some authors have designed Mn-doped CDs as dual modal FL/MR CAs and tested their performance with promising results. For instance, Ji et al. synthesized Mn-doped CDs citric acid and urea for the detection and intra-operative location of small brain gliomas. They presented a green emission with a QY of 10%. As for their MR performance, a r_1 relaxivity of 6.23 $mM^{-1}s^{-1}$ was reported. The probes were tested both *in vivo* and *ex vivo* to probe their targetability towards organs with high levels of blood flow.[126] In another recent work, Irmania et al. manufactured Mn-doped and further FA and chlorin e6 (Ce6) conjugated CDs from waste green, not only for diagnosis but also for therapy. This nanohybrid had no significant toxicity while showing a photodynamic therapy effect after 5 minutes resulted in the death of more than 90% of the cells. r_1 and r_2 were 13.88 and 80.04 $mM^{-1}s^{-1}$, respectively.[127] Likewise, Yao et al. doped CDs, obtained from waste crab shell, with Gd, Mn and Eu for bioimaging. CDs provided a r_1 of 4.78 $mM^{-1}s^{-1}$, which is higher than commercial agents, while Mn and Eu-doped CDs exhibited r_2 values of 140.7 $mM^{-1}s^{-1}$ and 29.32 $mM^{-1}s^{-1}$, respectively. Gd-doped CDs were further targeted to folate receptors by conjugating folic acid (FA) and then adapted with doxorubicin (DOX) to develop a potential drug delivery vehicle.[6] Rub Pakkath et al. fabricated and further loaded ethylenediamine (EDA) CDs from Citrus limon extract with a series of transition metal ions (Mn^{2+}, Fe^{2+}, Co^{2+} and Ni^{2+}) for bioimaging. The transition metal ions-doped CDs showed enhanced PL and efficient T_1-contrast with the highest QY being 75.07%, for Co-doped CD, and the maximum r_1 value of 0.341 $mM^{-1}s^{-1}$ and r_2 was 2.015 $mM^{-1}s^{-1}$ for Mn-doped CDs. Moreover, they confirmed their excellent biocompatibility in human colon cancer cells (SW480).[128] In addition, Lin et al. synthesized novel P and Mn dual-doped, where the role of the additional P^{3+} dopant was to enhance the emission

efficiency. Further conjugation with hyaluronic acid (HA) endowed them with tumor cell selectivity towards CD44-overexpressing cancer cells. Its MR imaging performance resulted in r_1 and r_2 values of 5.49 and 64.12 $mM^{-1}s^{-1}$, respectively.[129] Other works have shown similar results.[6,130,131]

1.5 Statement of the Problem

Molecular imaging has gained significant attention due to its ability to monitor biological processes and identify any structural, functional, or molecular abnormalities at the cellular and molecular level, leading to diagnose diseases in real time with a non-invasive approach.[46] Among these techniques, MR imaging is one of the most popular because it provides high spatial resolution and good contrast without the need of ionizing energy. However, one of its main drawbacks is that it lacks in sensitivity. As a consequence, it is difficult to obtain accurate and fast results.[132] On the other hand, FL imaging, another popular technique, can provide high cellular and subcellular sensitivity hence addressing the poor sensitivity of MR. imaging.[27] Thus, by combining these two techniques it is possible to design multimodal magnetofluorescent probes that can improve diagnostic performance and lead to faster and more accurate results in clinical diagnosis.[7] As a response, efforts have been made to develop magneto-fluorescent probes based on nanomaterials to improve efficiency and specificity. Despite that, most of the synthetic and post-synthetic surface modification methods are lengthy, costly, and require the use of organic solvents.[6]

Among the continuously increasing variety of nanomaterials, CDs have attracted attention owing to their low-cost, rapid, and environmentally friendly synthetic routes. Plus, they can provide bright fluorescence, high water dispersibility, good photo and chemical stability, and an excellent biocompatibility. In the past years, Gd-based CAs have been translated to the nanoscale

in the form of CDs. Nonetheless, the use of Gd in contrast agents has raised concerns after being associated to the development of NSF.[54] Furthermore, due to the lack of sensitivity of MR imaging, high concentrations of CAs are typically administered. As such there is a growing need to develop safer probes. As an alternative, Mn^{2+} has attracted attention due to its magnetic properties resembling those of Gd^{3+}. Unlike Gd^{3+}, Mn^{2+} can be naturally found in the body. In addition, it can form thermodynamically and kinetically stable complexes with chelators such as cDTPAA.[125]

Within this framework, some authors have designed Mn-doped CDs as dual modal FL/MR CAs and tested their performance both in vitro and in vivo with promising results.[6,126,128–131] However, there is still a challenge to construct probes that can be excited at long wavelengths, to avoid autofluorescence, and that can provide a contrast enhancement at low doses, to prevent cytotoxic effects.[121,131]

Herein, magneto-fluorescent CDs were developed for their potential application in FL/MR dual-modal imaging. The carbon dots can concomitantly fluoresce in the blue and red regions of the spectrum. The longer wavelength red fluorescence can be independently excited using $\lambda_{exc} >$ 640 nm to circumvent the need for short excitation wavelengths. Taking advantage of the amine groups in the surface of the as-synthesised fluorescent CDs, Mn^{2+} was coordinated through the mediation of DTPA, a well-known chelator, to form CDs-cDTPAA-Mn. The conjugation protocol was optimized to ensure that the final probe would provide an enhanced contrast in MR imaging, with a minimal metal loading while maintaining significant fluorescent properties. In this sense, both the optical properties and MR performance were evaluated together with cytotoxicity studies to confirm its potential biological application as an alternative imaging probe. Moreover, the possibility to excite CDs-cDTPAA-Mn at a 640 nm wavelength will contribute to reduce the autofluorescence in fluorescence imaging.[3]

2 Materials and Methods

2.1 Chemicals and reagents

All chemicals were obtained from commercial sources and were of analytical grade. Formamide (≥ 99.5%), L-glutathione (≥ 98.0%), and acetic anhydride (Certified ACS, ≥ 97.0%) were purchased from Thermo Fisher Scientific. Diethylenetriaminepentaacetic acid (DTPA) (98+%) and manganese (II) chloride ($MnCl_2$) (97%) were acquired from Acros Organics. Diethyl ether anhydrous (ACS reagent, ≥ 99.0%) containing BHT as inhibitor, and phosphate buffered saline (PBS) were purchased from Sigma-Aldrich. Spectra/Por cellulose ester dialysis membrane (MW cutoff 3.5-5. kDa) was. obtained from Spectrum. Pyridine (99+%) was purchased from Alfa Aesar. 1-Ethyl-3-(3-dimethylaminopropyl) carbodiimide hydrochloride (EDC) (> 99%) was acquired from AK Scientific. Nitric acid was purchased from Caledon. Water was ultrapurified (18.2 MΩ·cm) by being passed through a Milli-Q® Direct 8 Water Purification System. All chemicals were used directly without any further purification.

2.2 Reactions

2.2.1 Synthesis of CDs

A well-stablished protocol was employed to synthesize CDs.[101,133,134] Briefly, in a typical experiment, a 20 mL solution of 0.1 M L-glutathione in formamide was prepared and sonicated for 15 minutes. The solution was reacted in a CEM Discover SP microwave at 180°C for 5 min under constant stirring. The solution was then dialyzed in Milli-Q water using a Spectra/Por® cellulose ester dialysis membrane (MW cutoff: 3.5-5.0 kDa) for five days with fresh water added

every day to remove any unreacted molecules. Following dialysis, the solution was concentrated in a rotary evaporator at 60°C for 30 minutes. The product was washed with acetone and ethanol and subjected to centrifugation at 10,000 x g for 10 minutes. Lastly, the precipitate was collected and dried overnight in an oven at 70°C. Figure 11 summarizes the CD synthesis protocol using microwave chemistry with subsequent purification and isolation steps of the dots.

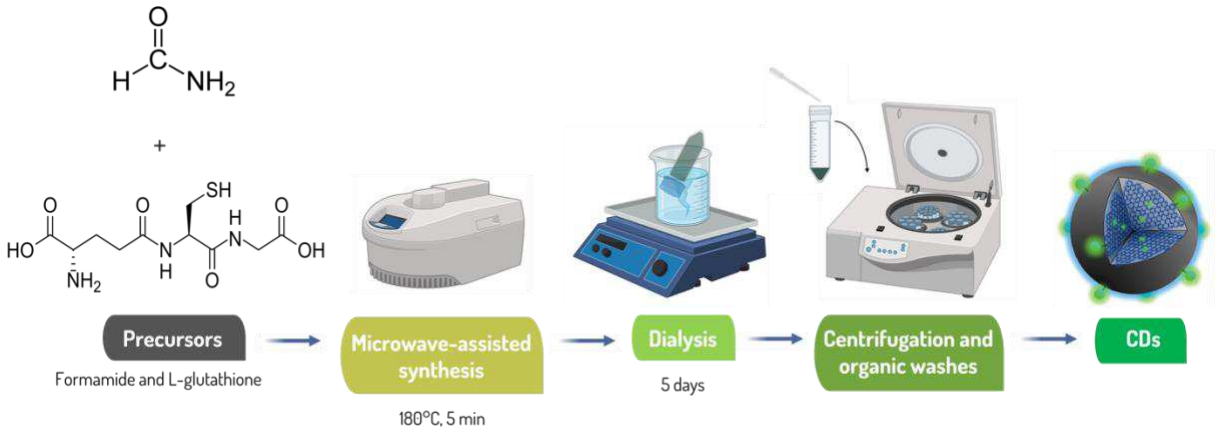

Figure 11. Synthetic procedure to obtain CDs from formamide and L-glutathione via a microwave-assisted technique at 180°C for 5 min.

2.2.2 Synthesis of cDTPAA

cDTPAA was obtained following the reported protocol by Paik et al.[135] First, 0.02 mol DTPA, 0.085 mol acetic anhydride and 0.15 mol pyridine were reacted under reflux and constant stirring at 65°C for 24 h. The products were then filtered and washed with acetic anhydride and ether. Lastly, the product was dried under ambient conditions.

2.2.3 Functionalization of CDs and optimization of the metal chelating protocol

A protocol established by Shi et al. was adopted to functionalize CDs with Mn^{2+}.[121] First, 83.96 µmol cDTPAA were reacted with 0.026 mmol EDC and 2 mL of a 5 mg/mL CDs dispersion in

PBS (pH 7.4) under constant stirring at room temperature. The mixture was allowed to react overnight to obtain CDs-cDTPAA. The reaction was followed by the addition of 0.79 µmol $MnCl_2$. While this concentration amounts to a 1 wt% Mn^{2+} loading, it is predicated on the assumption that the metal has fully chelated to the surface of the CD. The actual (i.e. real) metal content of the samples was elucidated by carrying out Inductive Coupled Plasma-Optical Emission Spectroscopy (ICP-OES) analyses. The product was then dialyzed in Milli-Q water using a Spectra/Por® cellulose ester dialysis membrane (MW cutoff: 3.5-5.0 kDa) during five days with fresh water each day. Finally, the suspension was dried in the oven at 70°C. For the optimization of this protocol, increasing concentrations of cDTPAA (83.96, 419.8, and 839.6 µmol) with a fixed amount of $MnCl_2$ were investigated. Alternatively, the amount of cDTPAA was kept constant while concentrations of $MnCl_2$ (1, 3, and 5 wt%) were varied for further experiments. Figure 12 summarizes this protocol.

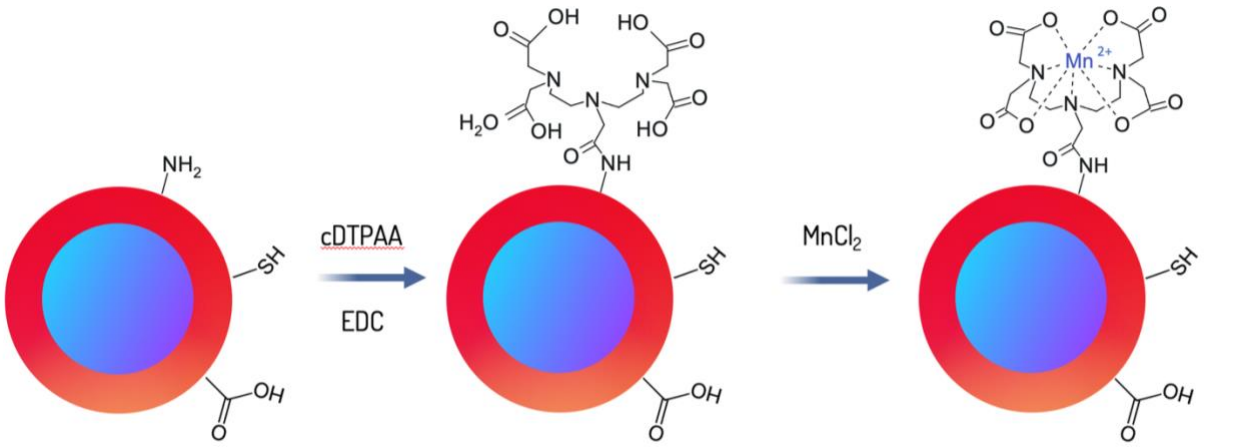

Figure 12. Scheme of the formation of CDs-cDTPAA-Mn from amine-terminated CDs.

2.3 Characterization

2.3.1 Transmission Electron Microscopy (TEM)

TEM grids (3.05 mm, 300 mesh copper grids) were prepared by pipetting 25 µL of a 5 $mg \cdot mL^{-1}$ CDs dispersion in Milli-Q water and isopropanol (4:1) onto the surface followed by evaporation of the solvent. TEM images were collected using a LVEM5 Benchtop Electron Microscope (Delong America) operating at 5.3 kV.

2.3.2 Powder X-ray Diffraction (PXRD)

XRD pattern of CDs were obtained using a D2 PHASER X-ray Analyzer (Bruker) with Cu·Kα radiation (λ =1.54184 Å) running at 30 kV and 10 mA. The diffractogram were recorded in the range of 2θ from 0 to 80°.

2.3.3 Ultraviolet-Visible (UV-Vis) Absorbance Spectroscopy

50 $\mu g \cdot mL^{-1}$ CDs dispersions were prepared. UV-Vis absorption spectra were recorded in a Cary 5 Series UV-Vis-NIR Spectrophotometer (Agilent Technologies) in the range from 200 to 800 nm using a 1 cm quartz cuvette. The bandwidth was set to 5 nm with a wavelength changeover at 350 nm.

2.3.4 Fluorescence Spectroscopy

50 $\mu g \cdot mL^{-1}$ CDs dispersions were prepared. Fluorescence spectra were measured using a Cary Eclipse Fluorescence Spectrophotometer (Agilent Technologies) at λex = 420 and 640 nm in a 1

cm quartz cuvette. The widths of the excitation and emission slits were both set to 5 nm, and PMT voltage to 600 V.

2.3.5 Fluorescence Quantum Yield (QY) Measurement

50 μg·mL^{-1} CDs dispersions were prepared. Fluorescence QY was then determined in a FL920 Fluorescence Spectrometer (Edinburgh Instruments) coupled to an integrating sphere in the range from 300 to 800 nm using a 1 cm quartz cuvette. Excitation and emission slit widths were set to 5 nm, excitation wavelength to 405 nm, with a dwell time of 0.2 s. Scans were carried out in triplicates.

2.3.6 Lifetimes Studies

Fluorescence lifetimes were obtained in an EasyLife X fluorescence lifetime system (Optical Building Blocks) using a 1 cm quartz cuvette with a 368 nm pulsed ps LED excitation. The emission slit width was set to 1.5 mm, channel number to 500, integration time to 0.25 s. Analysis of 50 μg·mL^{-1} CDs dispersions were carried out in triplicate.

2.3.7 Photostability Studies

Photostability was evaluated by exposing 50 μg·mL^{-1} CDs dispersions to a longwave-UV light (365 nm) for 0, 0.5, 1, 2, 3, 6, 12 and 24 h. UV illumination was applied using a Chromato-Vue C-70G UV Viewing System. Fluorescence spectra were then recorded at λ_{ex} = 420 and 640 nm using a 1 cm quartz cuvette in a Cary Eclipse Fluorescence Spectrophotometer (Agilent Technologies). The width of the excitation and emission slits was set to 5 nm with a PMT voltage of 600 V.

2.3.8 Attenuated Total Reflectance Fourier-Transform Infrared Spectroscopy (ATR-FTIR)

FTIR spectra were recorded in a Thermo Scientific Nicolet iS5 coupled to an iD5 ATR accessory. Spectra were collected using 100 scans with a resolution of 16 cm^{-1}, a gain of 1, an optical velocity of 0.4747, and an aperture setting of 100.

2.3.9 X-ray Photoelectron Spectroscopy (XPS)

X-ray Photoelectron Spectroscopy (XPS) of CDs was performed using an A1 Kα X-ray Photoelectron Spectrometer (Thermo Fisher Scientific). High-resolution and survey scans from 10 runs were resolved. Measurements were conducted in triplicates.

2.3.10 Surface Zeta (ζ) Potential Measurements

50 $\mu g \cdot mL^{-1}$ CDs dispersions were used for all ζ potential measurements. Analyses were carried out using a Nano-ZS90 Zetasizer (Malvern) with a disposable folded capillary cell. Measurements were performed in triplicate at 25°C.

2.3.11 Inductive Coupled Plasma Optical Emission Spectroscopy (ICP-OES)

Metal loading was assessed using a 5100 ICP-OES system (Agilent). All CDs samples were digested in 1% HNO_3. Three analytical wavelengths were used for analysis namely 257.610, 259.372, and 260.568 nm. Argon was used for plasma generation and nebulization with a power of 1.2 kW. Plasma flow and nebulization flow rates of 12 and 0.7 L/min were used, respectively.

2.3.12 Relaxivity measurements

1 mL CDs solutions and subsequent 3:4, 1:2, 1:4 dilutions were prepared in a 96-well plate. MR scanning images were collected in an M2 1 T MR imaging system (Aspect Imaging). T_1-weighted spin-echo sequence was performed with the following parameters: TE = 11 ms, TR = 400 ms, fα = 90°; FOV = 50 x 50 mm, slice thickness = 0.9 mm s, gap = 0.1 mm gap, dwell time = 16 μs, matrix size = 256 x 256, excitations = 5.

2.3.13 Cell Viability

2.3.13.1 Cell Culture

Human colorectal adenocarcinoma (HT-29) cells were cultured in in Dulbecco's modified Eagle medium (DMEM) supplemented with 10% fetal bovine serum (FBS). and incubated at 37°C in a humidified atmosphere with 5% CO_2.

2.3.13.2 Cytotoxicity Studies

Cytotoxicity of CDs was investigated in HT-29 cell lines by an MTS assay. Cells were seeded in a 96-well culture plate at a density of 2000 cells per well in culture medium and incubated at 37°C for 24 h. Cells were then treated with varying concentrations of CDs (50, 100 and 250 $\mu g \cdot mL^{-1}$), and incubated again for 24 h. Then, the culture medium was replaced with 200 μL of fresh complete medium and incubated once again for 24 h. After 24 h, the MTS reagent was added and incubated at 37°C for 2 h. Absorbance values were read with a Multiskan GO microplate spectrophotometer (Thermo Scientific) at a λ=490 nm. Experiments were performed in triplicates.

2.3.14 Neutron Activation Analysis (NAA)

NAA was carried out to monitor the release of metal ions over time using a SLOWPOKE reactor. 50 $\mu g \cdot mL^{-1}$ CDs dispersions were continuously dialyzed in Milli-Q water using a Spectra/Por® cellulose ester dialysis membrane (MW cutoff: 3.5-5.0 kDa). Aliquots of the dialysis product were collected for analysis every day for 7 days. Neutron activation analysis (NAA) is a technique to determine different elements based on the conversion of a stable nuclei to a radioactive nuclei through a nuclear reaction triggered by gamma radiation. The reaction rates to produce radioactive isotopes are characteristic of every element. The instrument measures the radioactivity released during the decay of the radionuclide which can be later translated into the number of nuclei of the stable isotope and will provide information about the mass, and the concentration of the element. This technique is mainly used for trace element analysis.[136] When compared to other techniques, for instance ICP-based techniques, NAA offers a remarkably higher sensitivity.[137]

3 Results and discussion

CDs were synthesized via a microwave-assisted technique. Unlike conventional heating, a microwave assisted technique offered faster reaction times, and more uniform heating.[138] The reaction proceeded in a 35 mL microwave vial containing the precursors, which were heated to 180 °C for 5 min and using a stirring setting of medium. Both formamide and L-glutathione were used as the carbon source and heteroatomic dopants.

3.1 Physical Properties

The morphology and size distribution of the as-synthesized CDs were characterized by TEM. Based on TEM analysis, CDs exhibited a quasi-spherical shape with an average size of 12.9 ± 3.1 nm and a relatively broad size distribution ranging from 4 to 20 nm (Figure 13a) with a few aggregates due to attractive intermolecular forces, most likely due to the formation of hydrogen bonds among the surface groups on their surface. In the absence of elements of high atomic numbers in the composition of the CDs and owing to a lack of long-range order, CDs exhibit poor contrast as evidenced by TEM. Following the addition of Mn^{2+} yields darker CDs with an average diameter of 32.1 ± 7.56 nm (Figure 13b) and no aggregation is observed presumably because of cations coordinating directly to the functional groups. The higher atomic number of the metal contributes to the enhanced contrast. On the other hand, upon conjugation with cDTPAA, TEM images (Figure 13c) revealed darker, more spherical, larger CDs with a mean size of 22.7 ± 7.1 nm and a few aggregates, evidencing an increase in size. Comparably, the formation of CDs-cDTPAA-Mn, resulted in nanoparticles (Figure 13d) with an average diameter of 28.6 ± 9.2 nm, showing that the surface modification of CDs resulted in an increase of 15 nm of their original size, suggesting a successful modification. No aggregation is observed, which might be again

attributed to the coordination of metals to the functional groups in this case of both CDs and cDTPAA. We noted that the chelation of Mn^{2+} via cDTPAA provided a lower contrast in the TEM indicating that the concentration of the chelated manganese cations is lower relative to the approach that relies on direct electrostatic interactions between the CD surface and the metal cation.

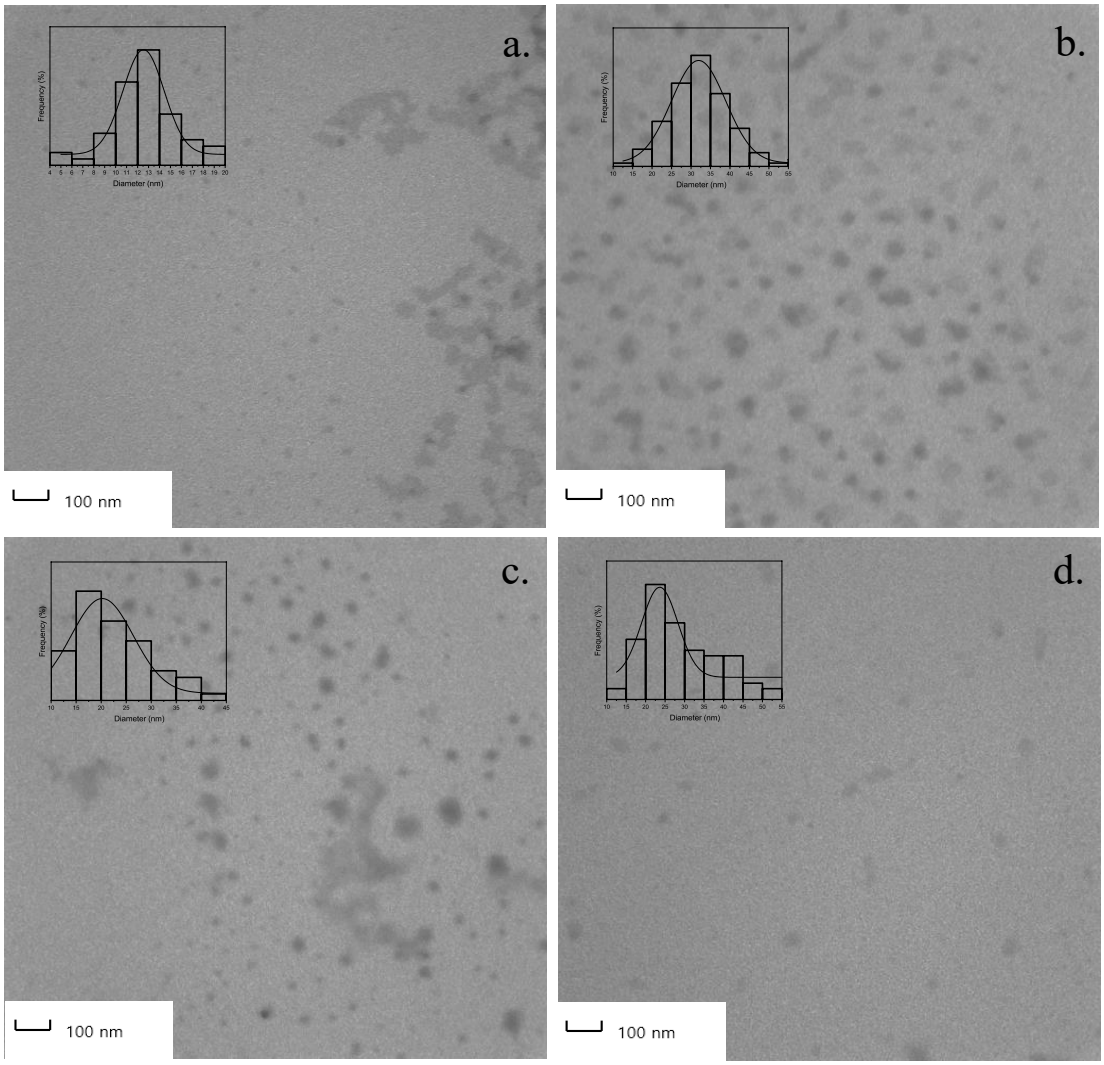

Figure 13. TEM images of (a) CDs, (b) CDs-cDTPAA (419.8 µmol), (c) CDs-Mn (3 wt %), (d) CD-cDTPAA (419.8 µmol)-Mn (3 wt%). Insets show the corresponding size distribution histograms.

In addition, PXRD was performed to determine the crystal structure of CDs. The X-ray diffractogram in Figure 14a revealed a broad band at a 2θ value of 23 ° corresponding to the (002) hkl plane. This signal has been broadly associated with the plane of graphite with an interlayer spacing of 0.32 nm. This suggests that CDs have a graphitic structure.[139,140] No other crystalline reflections were observed in the diffraction pattern speaking to a predominantly amorphous nature of the dots. On the other hand, when compared to one of the precursors, it is observed that L-glutathione has a clearly defined crystalline pattern showing multiple reflections. As expected, these reflections are not observed in the PXRD pattern of the purified dots. Conversely, after conjugation with cDTPAA, the resulting PXRD pattern resembled that of cDTPAA, suggesting a change in the crystalline structure of CDs (Figure 14b). Thus, indicating a successful functionalization.

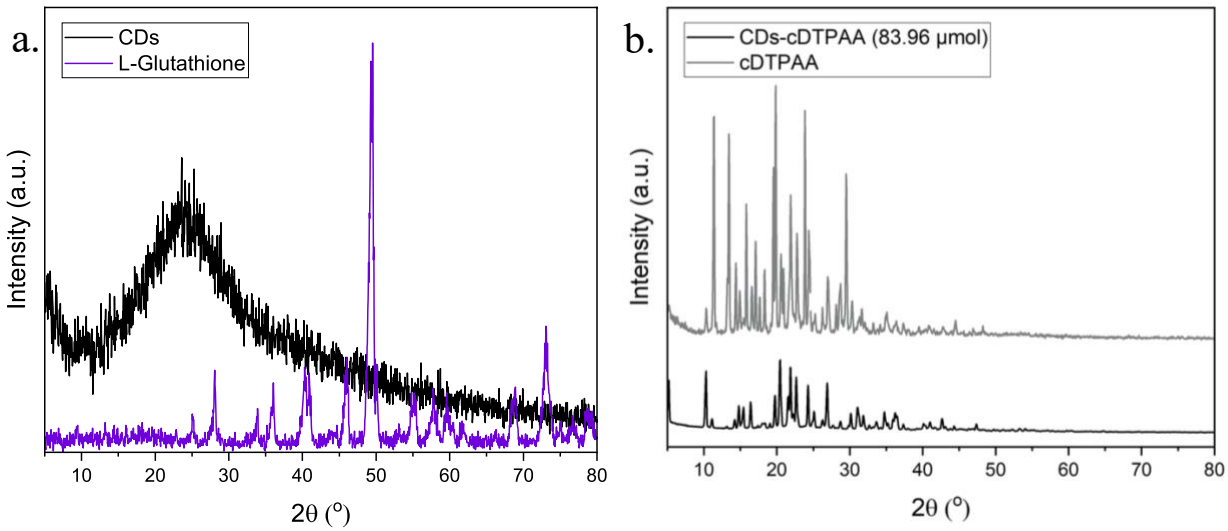

Figure 14. X-ray diffraction pattern of (a) CDs showing a broad reflection at around 23° 2θ associated with a graphitic structure. In contrast, X-ray diffraction pattern of L-glutathione shows a series of sharp reflections associated with well-defined long range order; and (b) functionalized CDs with well-defined long range order, resembling the X-ray diffraction pattern of cDTPAA.

To the best of our knowledge, confirmation of functionalization with cDTPAA using XRD has not been reported before. Hence, this approach could be a primary strategy to do so.

3.2 Optical Properties

The optical properties of the dots and modified constructs were investigated using absorption and fluorescence spectroscopies. As seen in Figure 15a, the UV-vis absorbance spectrum of CDs displays three bands. The first band is centered around 325 nm and could be assigned to the $\pi \rightarrow \pi*$ transition of the conjugated C=C bonds, suggesting the presence of an aromatic ring structure that is formed during the carbonization process. The second band is centered around 420 nm and could be associated with the $n \rightarrow \pi*$ transition of the C=O bonds, ascribed to a trapped excited state energy. The third band spans 580 to 690 nm and could be attributed to the $n \rightarrow \pi*$ transitions of the C=N/C=S bonds.[104] In contrast, none of the precursors exhibit absorbance bands (Figure 15a) suggesting that the observed optical properties are solely attributed to the formation of the CDs. The absence of an absorption signal from the precursors in the 250-800 nm range results from a reduced delocalization of the π orbitals of the formamide and L-glutathione molecules, usually ascribed to C=C bonds.[141]

As seen in Figure 15a, when excited at 405 nm, CDs exhibit a dual fluorescent signal in the blue and the red regions of the UV-vis spectrum centered at 460 and 680 nm, respectively. On the other hand, when excited at 640 nm, only one fluorescence band is observed in the red region. The origin of the blue signal has been studied in-depth and was attributed to the carbon core while the red signal is believed to originate from the surface states.[101] It is noteworthy to mention that the red fluorescence is of particular interest for this work given the potential of these CDs in

biological applications and knowing that longer wavelengths of light can help circumvent the issues of autofluorescence and limited tissue penetration.

Both CDs as well as dots decorated with cDTPAA chelating Mn^{2+}, were highly dispersible in water and remained stable over several months with no signs of aggregation at ambient conditions. When dispersed in water at a concentration of 50 $\mu g \cdot mL^{-1}$, they form transparent colloidal dispersions, which upon exposure to UV light, evidence a bright blue fluorescence, as shown in Figure 15a inset. The observed blue fluorescence differs relative to the unmodified carbon dots which evidence a more violet colour following excitation using the same UV wavelength. The predominant blue color stems from the fact that chelation and coordination with the metal cations results in a decrease of the red fluorescence band relative to the blue counterpart

Similar to the unmodified CDs, the CDs-cDTPAA-Mn complex displays three bands in the UV-vis absorption spectrum. The first band centered around 325 nm, assigned to the $\pi \rightarrow \pi*$ transition of the conjugated C=C bonds, does not significantly change (Figure 15b), suggesting that the core structure is unaffected by chelation and coordination of the metal cation. As a result of the formation of the complex, a second band appears centered around 400 nm, which is associated with the $n \rightarrow \pi*$ transition of the C=O bonds and is supported by the absorption spectrum of CDs following conjugation with cDTPAA. Likewise, there is a formation of a third band which spans from 615 to 730 nm and could be attributed to the $n \rightarrow \pi*$ transitions of the C=N/C=S bonds. The third band could be correlated to the formation of a non-radiative complex and is supported by the absorption spectrum of CDs after direct coordination with Mn^{2+} without a chelator, which is shown in Figure 15b.

Fluorescence studies confirm that following conjugation with cDTPAA and further chelation with Mn^{2+}, a loss in signal intensity is observed (Figure 16a). Interestingly, only the red

band shows this decrease in intensity, suggesting that the surface states are solely affected. According to the literature, this is most likely due the formation of a non-emissive complex that translates into the transition between an emissive state to the ground state without the emission of a photon.[128142] Oppositely, if the Mn^{2+} is directly coordinated to the surface of the CDs, it will result in a completely quenched red fluorescence signal. This further supports that hypothesis that nonradiative recombination results from electron transfer between CDs and Mn^{2+}.

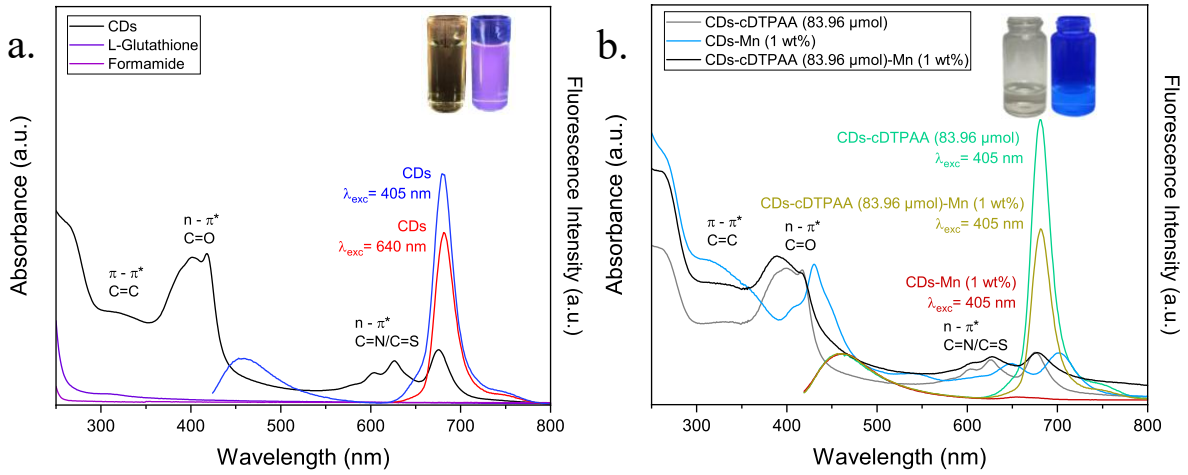

Figure 15. Absorption and fluorescence spectra of (a) CDs showing three absorptions bands at 250, 420 and 580-690 nm ascribed to the C=C, C=O and C=N/C=S functional groups, respectively. CDs exhibiting fluorescence emission at the blue and the red region of the UV-Vis spectrum when excited at 405 nm, stemming from the core and molecular states, respectively. When excited at 640 nm only red fluorescence is observed. Inset at the top right of (a) showing optical image of CDs following illumination using ambient light (left) and UV light (365 nm) (right); and (b) CDs conjugated with cDTPAA, CDs coordinated with Mn^{2+}, and CDs-cDTPAA-Mn complex showing formation of the three different absorptions bands at the same regions attributed to the C=C, C=O and C=N/C=S functional groups, respectively, due to the modification of the chemistry surface. CDs showing the effect of conjugation, metal coordination, and metal chelation on the red fluorescence emission when excited at 405 nm. Inset at the top right of (b) showing optical image of CDs-cDTPAA-Mn following illumination using ambient light (left) and UV light (right).

In contrast, the sole conjugation of cDTPAA leads to a slight increase in the red fluorescence signal, suggesting that the surface states are affected by the addition of more

delocalized functional groups. This affirmation can be supported by the fact that the blue fluorescence signal, originating from the carbon core, remains unchanged after conjugation, and further chelation of the metal ion. In this context, the role of cDTPAA is to mitigate the quenching effects caused by the direct addition of Mn^{2+} ions, paving the way for the development of a dual-modal probe using this type of strategy. For these reasons, we will focus on CDs-cDTPAA-Mn complexes rather than CDs-Mn.

This work focused on optimizing the conditions of the functionalization protocol with the goal of complexation of paramagnetic ions and thus endowing magnetic properties to the CDs while maintaining their fluorescent properties. Another reason to carry out fluorescence spectroscopy studies was to investigate how modifying the concentration of chelator and the concentration of metal salt in the reaction would affect the optical properties of the resultant functionalized CDs. To that end, CDs were first reacted with a fixed concentration of $MnCl_2$ (1 wt%) with increasing concentrations of cDTPAA of 83.96, 419.8, and 839.6 μmol. Figure 16a suggested that higher concentrations of cDTPAA allowed for more chelation sites, and hence a higher concentration of Mn^{2+} ions were loaded onto the surface of the CDs. In consequence, the relative fluorescence intensity decreased gradually because of the previously mentioned formation of the nonradiative complex. In parallel, the effect of the concentration of $MnCl_2$ was investigated. In this case, CDs were reacted with the same concentration of cDTPAA (83.96 μmol) while increasing concentrations of $MnCl_2$ were tested (1, 3, and 5 wt%). Even though the number of chelation sites remains unchanged, the addition of more metal ions would likely increase the probability of coordination to the chelating sites available. Correspondingly, higher concentrations of $MnCl_2$ led to a more evident quenching effect of the fluorescent signal (Figure 16b). It is also

possible that non-quencher mediated interactions occurred between the metal cation and the CD surface further resulting in quenching at higher metal concentrations.

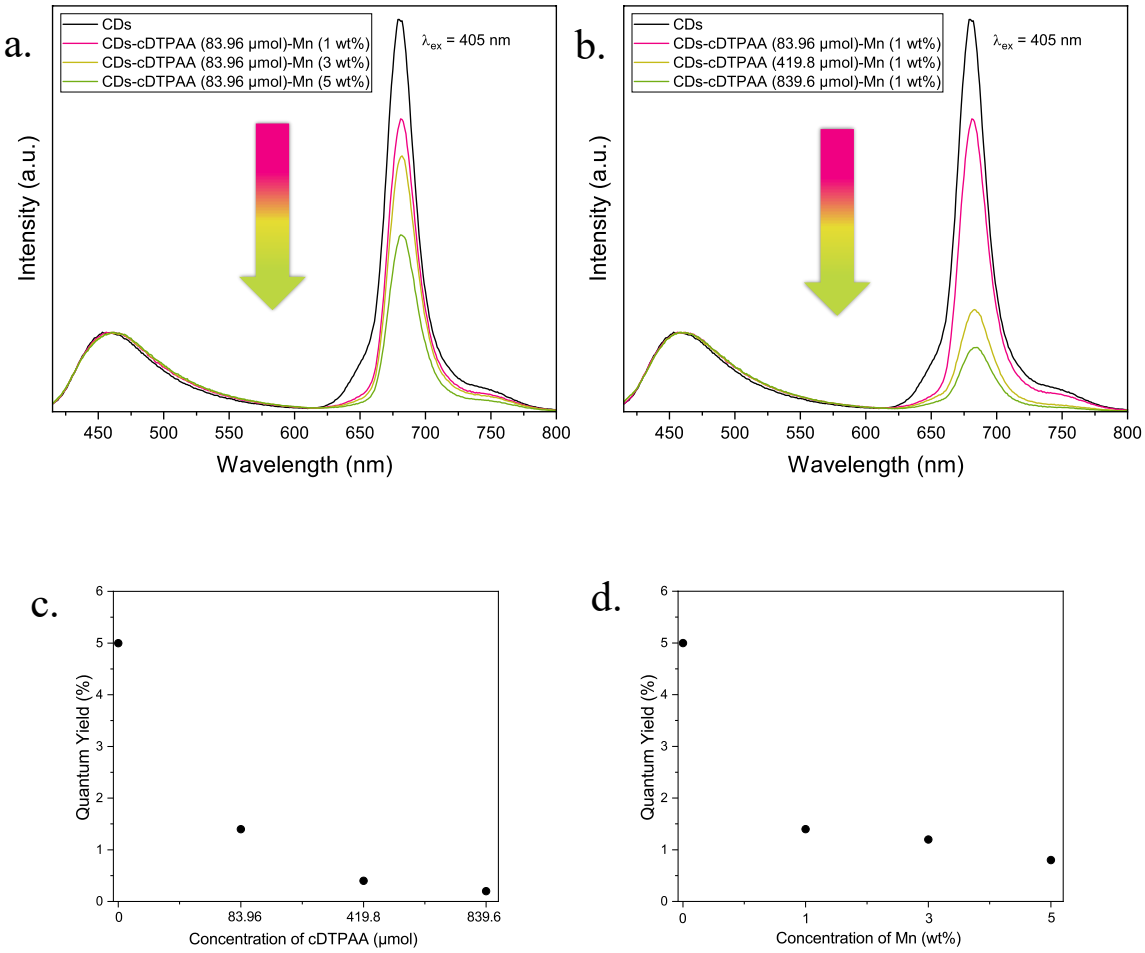

Figure 16. Fluorescence spectra showing: (a) changes in the relative intensity of functionalized CDs as a function of increasing concentrations of cDTPAA (83.96, 419.8, and 839.6 µmol), (b) changes in the relative fluorescence intensity of functionalized CDs as a function of increasing concentrations of $MnCl_2$ salt (1, 3, and 5 wt%). Quantum yields of functionalized CDs as a function of (c) increasing concentrations of cDTPAA (d) increasing concentrations of Mn^{2+}.

The fluorescence efficiency was assessed by measuring the QY of the CDs. The QY of the parent CDs was measured to be 5.0%. This value is in line with other works in the literature, which

have successfully used CDs in bioimaging, both in vitro and in vivo, with QYs ranging from 0.2% to 10%.[143144145] Following functionalization of the dots, their ability to emit photons is affected, as previously discussed before. Measured QYs ranged between 0.25 and 1.40% (Figure 16c and 16d) and while these are several folds lower than the parent dots, the CD-cDTPAA-Mn complex remains in the range of QYs suitable for molecular imaging applications. Alternatively, the direct coordination of metal ions resulted in QY values of ~0%, as evidenced by fluorescence spectroscopy studies and is attributed to the strong quenching effects. Low quantum yields are related to a rapid depopulation of the excited state by non-radiative processes.

In addition, lifetimes were measured to better understand the photoluminescence mechanism of CDs resulting from functionalization. The parents exhibited two fluorescence lifetimes measured as 0.2 ns (lifetime 1) and 4.7 ns (lifetime 2). As previously discussed, they have been associated with the red and blue fluorescence, namely, the electron-hole recombination in the molecular states, and the relaxation of the electrons from the core, respectively.[103] Table 1 shows the variation of lifetimes of functionalized CDs as a function of varying concentrations of both chelator and metal salt in the reaction. These findings suggest that the lifetime corresponding to the blue fluorescence is barely affected, almost negligible, since it is correlated to the core states. Conversely, the surface states seem to slightly prolong their lifetimes which could be beneficial for bioimaging. According to the literature, the reason for this increase in lifetime might be ascribed to a structural change of the CDs resulting from the formation of a covalent bond with cDTPAA. This structural change was confirmed by PXRD studies. Hence, a structural modification contributes to decrease the internal conversion (non-radiative decay process). At the same time, an increase in lifetime may suggest a dynamic quenching through a FRET mechanism

where the dipole-dipole interactions take place between the metal cation (acceptor) and the excited-state CDs (donor).[142,146,147]

Moreover, based on changes in the fluorescence spectra and modest to little change in fluorescence lifetimes, it is likely that quenching occurs through a static quenching mechanism in which a nonfluorescent ground state complex is formed when CDs interact with Mn^{2+}.[103148]

Table 1. Summary of calculated lifetimes for CDs, cDTPAA conjugated CDs, and further metal chelated CDs.

Sample	Lifetime 1 (ns)	Lifetime 2 (ns)
CDs	0.2	4.7
CDs-cDTPAA (83.96 µmol)	0.1	3.8
CDs-cDTPAA (419.8 µmol)	0.1	5.8
CDs-cDTPAA (839.6 µmol)	0.1	6.1
CDs-Mn (1 wt%)	0.2	5.0
CDs-Mn (3 wt%)	0.2	5.0
CDs-Mn (5 wt%)	0.2	5.1
CDs-cDTPAA (83.96 µmol)-Mn (1 wt%)	0.2	4.8
CDs-cDTPAA (83.96 µmol)-Mn (3 wt%)	0.2	4.8
CDs-cDTPAA (83.96 µmol)-Mn (5 wt%)	0.2	4.9
CDs-cDTPAA (419.8 µmol)-Mn (1 wt%)	0.1	6.2
CDs-cDTPAA (419.8 µmol)-Mn (3 wt%)	0.1	7.6
CDs-cDTPAA (419.8 µmol)-Mn (5 wt%)	0.1	7.6
CDs-cDTPAA (839.6 µmol)-Mn (1 wt%)	0.1	4.8
CDs-cDTPAA (839.6 µmol)-Mn (3 wt%)	0.1	4.8
CDs-cDTPAA (839.6 µmol)-Mn (5 wt%)	0.2	4.8

The photostability of the functionalized CDs was assessed by exposing them to continuous UV-vis irradiation during 24 h under different conditions, and the relative fluorescence intensities were fitted using a Gaussian function and compared (Figure 17). Firstly, the studies were carried

out at ambient (~20° C) and physiological (~37 °C) temperatures in ultrapure water. When compared, these findings indicated that the fluorescence properties of CDs are temperature dependent. By increasing the temperature, the relative intensity slightly decreases likely due to thermal activation of nonradiated trapping. In this sense, by increasing the temperature, nonradiative channels activate trapping by surface states. An increase in the quenching effect with an increase in temperature might confirm the hypothesis of dynamic quenching through a FRET mechanism.[142,149] At both ambient and physiological conditions a similar fluorescence profile is observed, with an exponential decrease after 6 hours of irradiation. During continuous irradiation over a period of 6 hours using a wavelength of light of 365 nm, we noted an exponential decrease in the fluorescence of the dots ascribed to photobleaching of the CDs.[150] In other words, the chemical structure of the CD-cDTPAA-Mn complex starts losing its ability to fluoresce. While photobleaching is not desirable, we do not envision impact on the potential application of this probe in fluorescence imaging since fluorescence imaging follows a real-time approach and does not require prolonged exposure to UV wavelengths.

The stability studies were also conducted in acidic (pH 3) and alkaline (pH 11) environments. It was noted that the complex is also pH dependent. An acidic environment resulted in a significant decrease of the relative intensity, while an alkaline environment triggered the opposite effect. This is due to the deprotonation and protonation of acidic and basic groups in the electronic states.[104] To date, the pH dependency mechanism of CDs has not completely elucidated, and is still a subject of debate due to the relatively complicated structure of CDs.[151] In terms of its potential biological application, this might suggest that the complex maintains its photoluminescent profile even under different conditions. The same exponential decay of the

fluorescence is observed after 6 hours for both cases. In this context, not only could the CDs-cDTPAA-Mn serve for bioimaging, but also for temperature and pH sensing.[104,105]

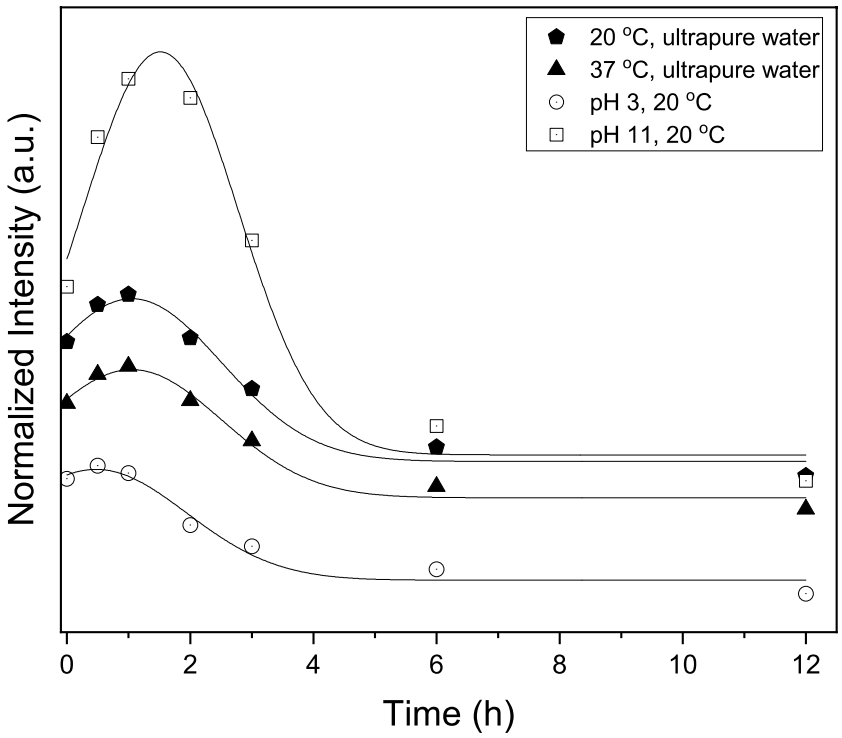

Figure 17. Photostability tests of CDs-cDTPAA-Mn under continuous irradiation with UV-light (365 nm) showing changes in the relative fluorescence intensity over a 24-h irradiation period at different conditions: 20 °C and 37 °C in ultrapure water; and pH 3 and 11 at 20°C.

3.3 Surface Properties

3.1.1 Surface Composition

The surface chemistry of the CDs was investigated by FTIR. As shown in Figure 18, the presence of O-H and N-H stretching vibrations from hydroxyl, carboxyl and amine groups can be associated with the broad band from 3000 to 3500 cm^{-1} which will serve for further functionalization. The presence of C=O, C-N, and C-O bonds is confirmed by the stretches at 1659, 1375, and 1297 cm^{-}

[1], respectively. The band at 1577 cm^{-1} can be assigned to the C=C/C=N bonds, which is consistent with previous works. [104] The surface composition of CDs is dependent on the choose of precursors, as depicted in Figure 18.

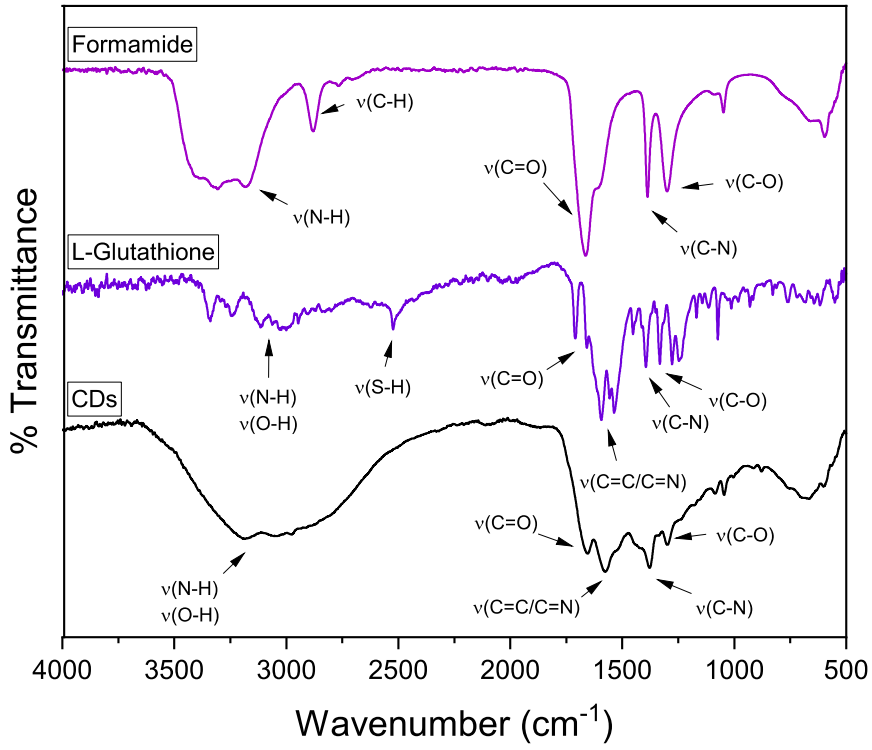

Figure 18. FTIR spectra of formamide, L-Glutathione, and CDs. A broad absorption band centered around 3250 cm^{-1} was ascribed to the stretching vibration of N-H and O-H. The bands at 1659, 1375, and 1297 cm^{-1} were associated to C=O, C-N, and C-O bonds, respectively.

From the FTIR spectra in Figure 19a, the formation of CDs-cDTPAA-Mn is confirmed by a slight shift of the C=O vibration from 1703 to 1659 cm^{-1} and the increase of its relative intensity and our findings are in agreement with those of Shi et al.[121] The decrease in wavenumbers could be explained by the formation of amide bonds between the carboxyl groups of cDTPAA and the amine groups in the surface of CDs, suggesting the successful formation of the complex through

covalent bonds. Moreover, the consumption of amine groups could be manifested by the decrease of the relative intensity of the broad band from 3000 to 3500 cm^{-1}. Moreover, the band at 3010 cm^{-1} corresponding to carboxyl O-H stretch stretching vibrations becomes observable due to the addition of carboxylate moieties. Nonetheless, the chelation of metal ions cannot be monitored by ATR-FTIR since vibrational frequencies of metals are out of the measuring range of the instrument, but they were tracked using XPS analysis (*vide infra*).

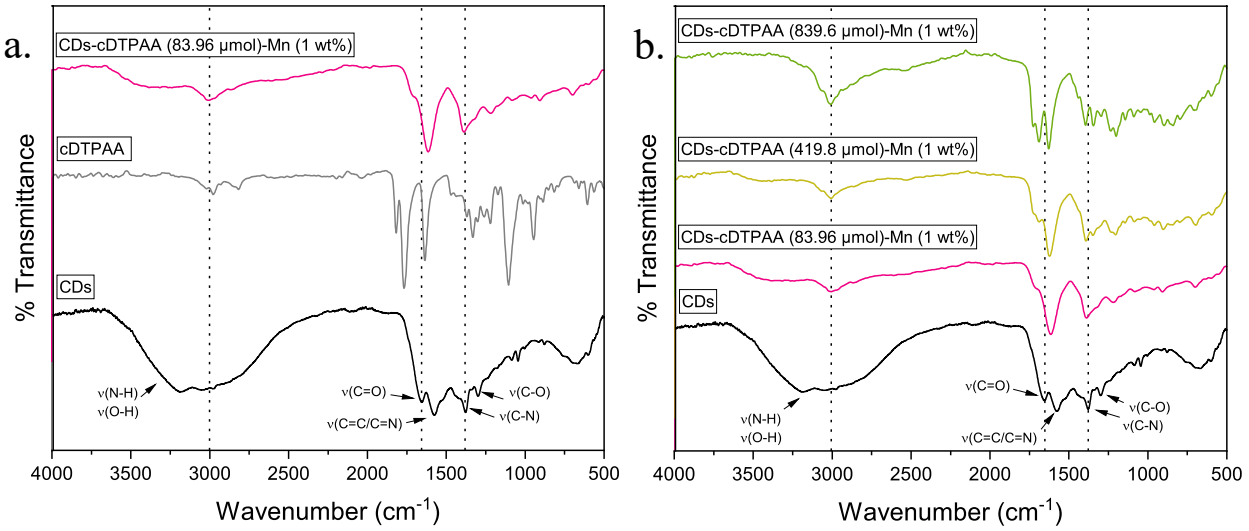

Figure 19. FTIR spectra of CDs showing **(a)** a reduction in wavenumber after cDTPAA conjugation for C=O groups from 1702.62 to 1658.96 cm^{-1}. cDTPAA is included as a reference. The direct coordination as wells as the chelation of metal ions is not observed since the vibrational frequencies of metals are out of the measuring range of the instrument; and **(b)** a reduction of the relative intensity of broad band from 3000-3500 cm^{-1}. The prominent band at 3010.33 cm^{-1} corresponding to O-H indicates a high concentration of cDTPAA molecules onto the surface of CDs.

We investigated the effect of varying the concentrations of cDTPAA in the functionalization reaction and the impact on the surface properties of the dots (Figure 19b). Increasing concentrations of cDTPAA translated into a gradual reduction of the relative intensity of broad band from 3000-3500 cm^{-1}, as previously highlighted. In this manner, fewer amine groups

were available after forming the CD-cDTPAA-Mn complex. On the other hand, the band at 3010 cm^{-1}, corresponding to carboxyl O-H stretch stretching vibrations, becomes more prominent. This could be correlated to the high concentrations of cDTPAA, which provides more chelation sites to capture more metal ions during the functionalization reaction.

In addition, X-ray Photoelectron Spectroscopy (XPS) was carried out to explore the chemical composition of CDs and CDs-cDTPAA-Mn. The XPS spectra of CDs (Figure 20a) exhibited five major binding energies at 531.1, 496.1, 400.1, 286.1 and 163.1 eV which are associated to O1s, Mn2p, N1s, C1s, and S2p, respectively. The calculated elemental composition for CDs was 54.01% carbon, 14.57% nitrogen, 29.53% oxygen, 1.5% sulfur.

The high-resolution XPS (HRXPS) spectra of each element are shown in Figures 20b-e. O1s HRXPS spectrum can be deconvoluted into two peaks, where 531.7 eV is assigned to C=O at, and 533.5 eV to C-OH/C-O-C. For N1s, two peaks are displayed at 400.2, and 402.2 eV suggesting a NH_2/pyrolytic and graphitic nature, respectively. Spectrum of C1s can be decomposed into 284.0, 285.8, and 287.7 eV which can be associated with C=C/C-C, C-N, and C=O/C=N, respectively. For, S2p three observable peaks 161.68, 163.28, and 164.70 eV associated to thiophene $S_{2p1/2}$, thiophene $S_{2p3/2}$, thiol, C-SO_2-C, and C-SO_3-H, respectively.

Similarly, functionalized CDs display the same bands for C1s, O1s, and S2p (Figures 20f,h,i). In addition to the two observable peaks at 399.6 and 402.3 eV ascribed to graphitic N, and pyrrolic N/NH_2, two bands are observed at 399.0, and 401.4 corresponding to C-N-C and N-H (Figure 20g). More notably, HRXPS Mn2p was deconvoluted in two peaks at 641.0, and 652.1 eV, corresponding to $Mn2p_{3/2}$ and $Mn2p_{1/2}$, respectively (Figure 20j). It is noteworthy to mention that the HR-XPS signals for Mn2p have a high degree of noise, which might be related to the limit of detection. XPS detection limits usually range between 1 and 0.1 at%. In this case, the CDs-

cDTPAA-Mn sample analyzed corresponds to 0.9 at% (or 5 wt%). Hence, the signal is evidently weak but still noticeable.

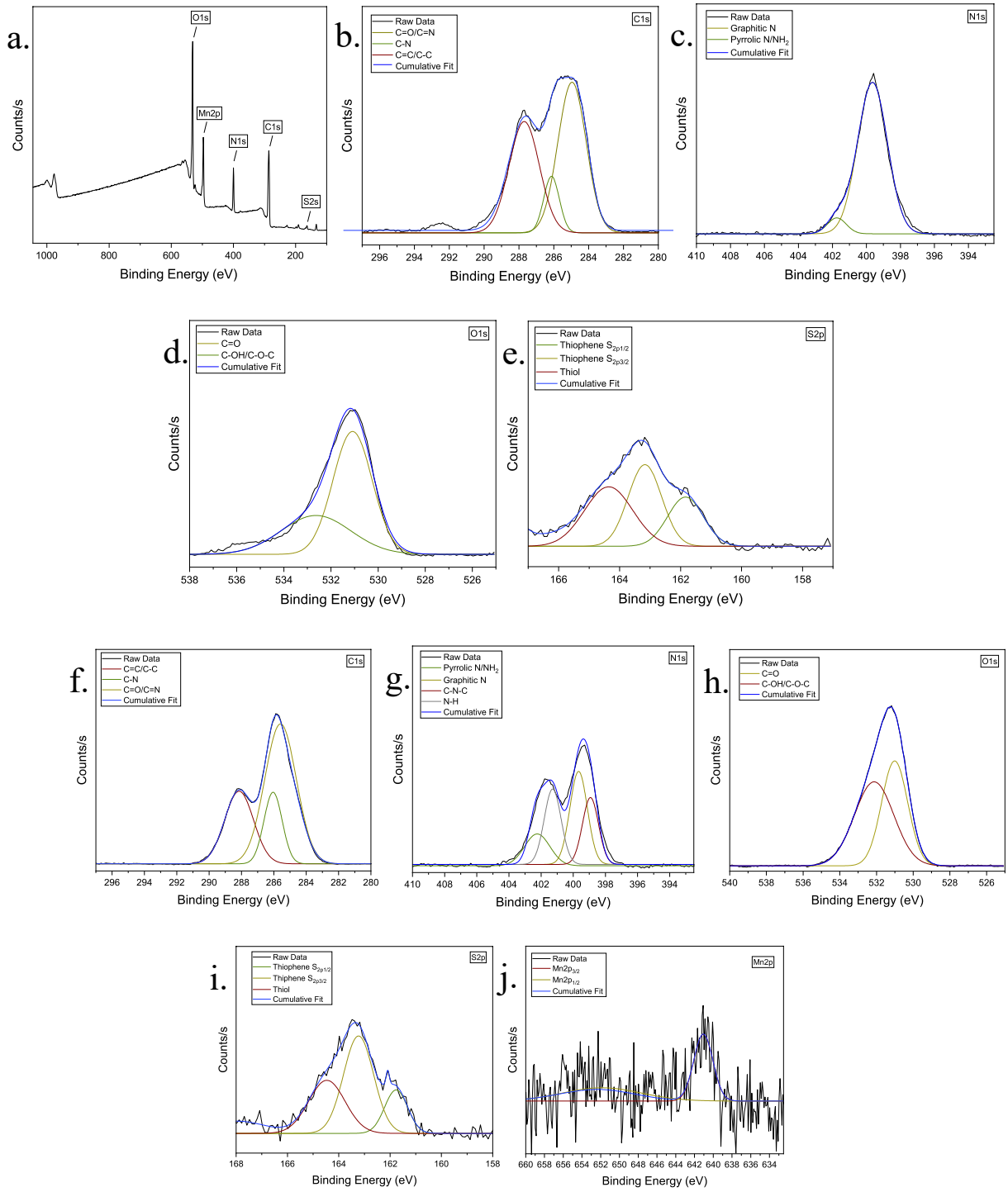

Figure 20. (a) XPS survey spectrum of CDs. Deconvoluted HR-XPS spectra of CDs: **(b)** C1s in 284.98, 285.79, and 287.68 eV corresponding to C=C/C-C, C-N, and C=O/C=N, respectively; **(c)**

N1s in 400.15, and 402.18 eV ascribed to pyrrolic N/NH_2, and graphitic N, respectively; **(d)** O1s 531.74, and 533.48 eV, assigned to C=O/C-O-C, and C=O, respectively; and **(e)** S2p in 161.68, 163.28, 164.70 eV, associated to thiophene $S2p_{1/2}$, thiophene $S2p_{3/2}$, thiol respectively. Deconvoluted HR-XPS spectra of CDs-cDTPAA-Mn: **(f)** C1s in 285.62, 286.04, and 288.09 eV corresponding to C=C/C-C, C-N, and C=O/C=N, respectively; **(g)** N1s in 398.96, 399.55, 401.37, and 402.28 eV ascribed to C-N-C, graphitic N, N-H, and pyrrolic N/NH_2, respectively; **(h)** O1s in 531.04, and 532.14 eV, assigned to C=O/C-O-C, and C=O, respectively; **(i)** S2p in 161.62, 163.26, and 164.68 eV associated to thiophene $S2p_{1/2}$, thiophene $S2p_{3/2}$, and thiol, respectively; and **(j)** Mn2p in 640.96, and 652.08 eV, corresponding to $Mn2p_{3/2}$ and $Mn2p_{1/2}$, respectively.

The calculated elemental composition for CDs-cDTPAA-Mn was 58.67% carbon, 12.32% nitrogen, 27.08% oxygen, 1.40% sulfur, 0.76% chlorine and 0.18% manganese. These findings agree with FTIR results.

3.3.2 Surface Charges

Zeta (ζ) potential measurements were conducted to investigate the changes in surface charges following conjugation of the CDs with cDTPAA and further chelation of Mn^{2+}. The surface zeta potential of the CDs was found to be -16.8 mV likely attributed to the negative carboxylic, hydroxyl, and amine moieties in their surface. Upon conjugation with cDTPAA, the surface ζ potential becomes more negative. This is triggered by the formation of an amide bond between the surface amine groups of the CDs and terminal carboxylate moieties of cDTPAA. Given that cDTPAA contains five carboxylates, one group reacts with the amine groups while the rest of the negatively charged groups remain unreacted. Further chelation with Mn^{2+} cations promotes the opposite effect. Upon the addition of Mn^{2+} cations, they are attracted by the unreacted negatively charged carboxyl groups of cDTPAA that are conjugated to the surface of CDs. By electrostatic attraction, Mn^{2+} ions are wrapped by the conformationally flexible molecule of cDTPAA whose chelation sites will share electrons with the cations to form a metal-coordinated complex. Thus,

the surface ζ potential becomes less negative. The change of ζ potential from CDs to CD-cDTPAA and then to CDs-cDTPAA-Mn suggested a successful formation of the complex.[121,152] Changes in ζ potential upon construction of CDs-cDTPAA-Mn can be tracked in Figure 21.

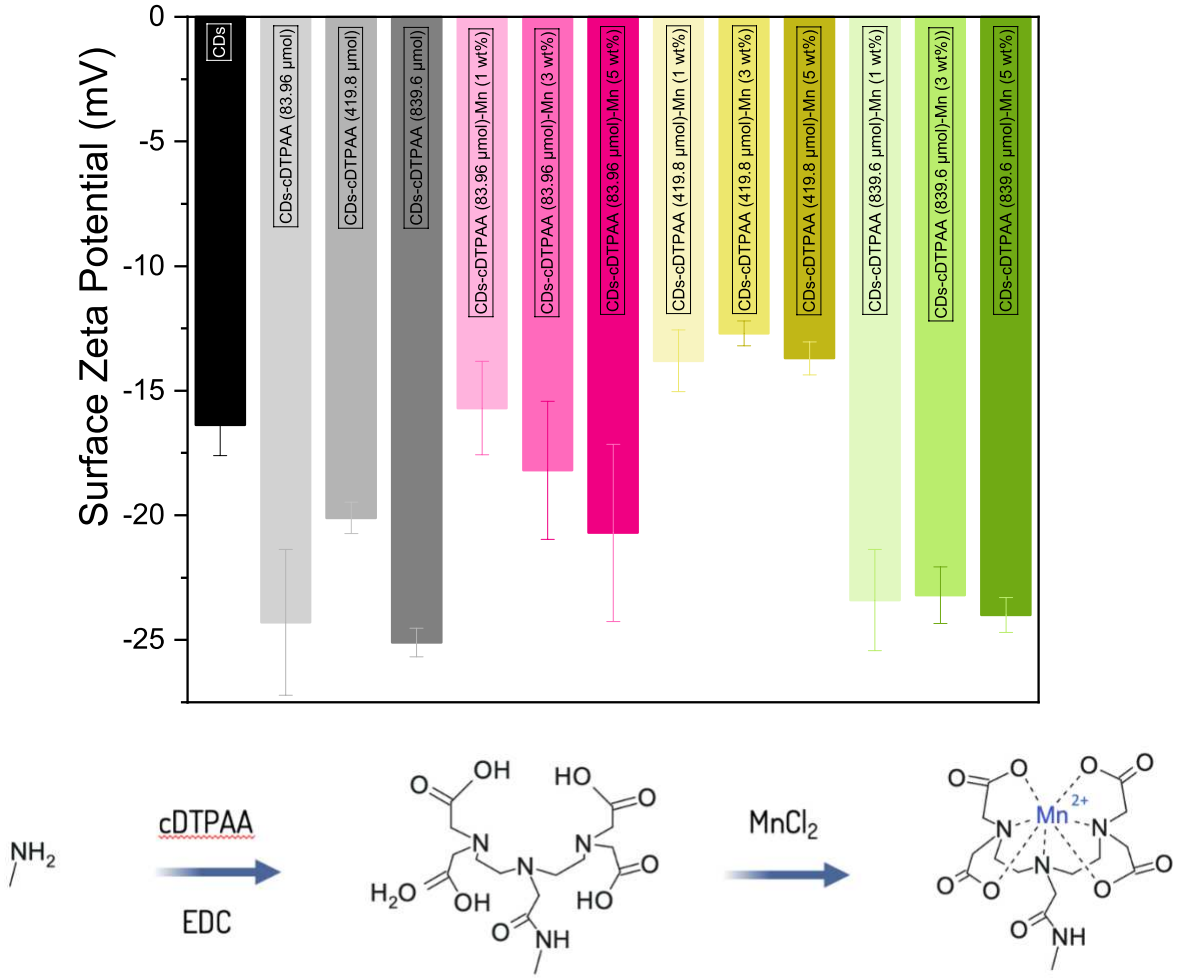

Figure 21. Surface ζ potential of CDs, CDs-cDTPAA, and CDs-cDTPAA-Mn as a function of varying concentrations of chelator and metal salt.

3.3.3 Surface Metal Loading

The loading of the Mn^{2+} cations onto the surface of CD-cDTPAA-Mn was evaluated using ICP-OES. Table 2 reveals that higher concentrations of cDTPAA are notably related to a higher

metal loading. This could result from an increased number of chelation sites available to coordinate more metal ions. By employing higher concentrations of metal salt in the reaction, more Mn^{2+} ions might occupy the available chelation sites. Table 2, for instance, reports the real Mn^{2+} content in terms of wt%. In light of this, the maximum Mn-loading achieved was 11 wt% at the highest concentration of cDTPAA, which is comparable to other works that have successfully developed probes that surpass the efficiency of traditional contrast agents.[121122] This demonstrates that this protocol is suitable to successfully integrate paramagnetic ions onto the surface of amine-terminated CDs.

Table 2. Mn^{2+} content on the surface of CDs, CDs-Mn, and CDs-cDTPAA-Mn as a function of varying concentrations of cDTPAA and Mn^{2+}.

Sample	[Mn^{2+}] (ppm)	Mn-Content (wt%)
CDs	0.00	0.00
CDs-Mn (1 wt%)	0.06	6.00
CDs-Mn (3 wt%)	0.07	7.00
CDs-Mn (5 wt%)	0.12	12.00
CDs-cDTPAA (83.96 µmol)-Mn (1 wt%)	0.01	1.00
CDs-cDTPAA (83.96 µmol)-Mn (3 wt%)	0.02	2.00
CDs-cDTPAA (83.96 µmol)-Mn (5 wt%)	0.04	4.00
CDs-cDTPAA (419.8 µmol)-Mn (1 wt%)	0.02	2.00
CDs-cDTPAA (419.8 µmol)-Mn (3 wt%)	0.04	4.00
CDs-cDTPAA (419.8 µmol)-Mn (5 wt%)	0.07	7.00
CDs-cDTPAA (839.6 µmol)-Mn (1 wt%)	0.08	8.00
CDs-cDTPAA (839.6 µmol)-Mn (3 wt%)	0.09	9.00
CDs-cDTPAA (839.6 µmol)-Mn (5 wt%)	0.11	11.00

In contrast, when Mn^{2+} ions are directly coordinated to the surface of CDs similar metal loadings are achieved. The difference is that more surface area is available for metal ions to

coordinate to the functional groups on the surface of CDs while the conjugation of large cDTPAA molecules limit the coordination sites in which metal cations can coordinate. The results in Table 2 agree with fluorescence spectroscopy findings, where higher concentrations of metal ions have proven to quench the fluorescence of CDs.

3.4 Magnetic Resonance Imaging Performance

Once the metal content in each of the resultant CDs-cDTPAA-Mn was elucidated, we carried out MR imaging studies to investigate the contrast enhancement that they could potentially provide to fulfill the main requirement of maintaining significant fluorescent properties along with significant magnetic properties. To investigate the suitability of CD-cDTPAA-Mn as potential MR imaging contrast agents, MR imaging *in vitro* was carried out. The longitudinal and transversal relaxivities of CDs-cDTPAA-Mn were calculated from the curve fitting of the T_1^{-1} and T_2^{-1} versus the concentration of Mn^{2+}, respectively.

Relaxivity values obtained were comparable to previous works where r_1 and r_2 values that range between 0.34 - 13.88 and 2.01 - 140.70 $mM^{-1}{\cdot}s^{-1}$, respectively, have been reported.[6,126–131] The relaxivity enhancement results from the coordination of Mn^{2+} to the surface of CDs. In the presence of Mn^{2+}, the relaxation rate of water would increase as a result of the dipole-dipole interactions between the protons and the applied magnetic field generated by the 5 unpaired electron spins of Mn^{2+}. When comparing the relaxivity values of directly metal coordinated CDs against the relaxivity values of metal-chelated CDs via cDTPAA conjugation, we noticed that even at similar metal loadings, the relaxivity values are not necessarily the same. The difference relies on the coordination number. Each Mn^{2+} atom has a coordination number of 6. Upon chelation, Mn^{2+} will coordinate to cDTPAA, where all donor atoms contribute to the coordination leaving

one coordination site where interactions with water molecules may occur. In contrast, in its non-chelated form, more coordination sites will be available for water molecules.[50]

Table 3. Relaxation parameters of CDs-cDTPAA-Mn at room temperature at a clinical field strength (1 T) using different concentrations of cDTPAA and Mn^{2+}.

Sample	r_1 ($mM^{-1}\cdot s^{-1}$)	r_2 ($mM^{-1}\cdot s^{-1}$)	r_2/r_1
CDs	0.003	0.005	1.4
CDs-Mn (1 wt%)	0.014	0.024	1.7
CDs-Mn (3 wt%)	0.041	0.105	2.5
CDs-Mn (5 wt%)	0.049	0.146	3.0
CDs-cDTPAA (83.96 µmol)-Mn (1 wt%)	0.009	0.017	1.9
CDs-cDTPAA (83.96 µmol)-Mn (3 wt%)	0.010	0.024	2.4
CDs-cDTPAA (83.96 µmol)-Mn (5 wt%)	0.013	0.042	3.3
CDs-cDTPAA (419.8 µmol)-Mn (1 wt%)	0.002	0.008	4.5
CDs-cDTPAA (419.8 µmol)-Mn (3 wt%)	0.002	0.010	4.7
CDs-cDTPAA (419.8 µmol)-Mn (5 wt%)	0.014	0.076	5.6
CDs-cDTPAA (839.6 µmol)-Mn (1 wt%)	0.002	0.017	7.7
CDs-cDTPAA (839.6 µmol)-Mn (3 wt%)	0.003	0.018	6.0
CDs-cDTPAA (839.6 µmol)-Mn (5 wt%)	0.010	0.052	5.5

The r_2/r_1 ratio determines whether a CA has the ability to produce a T_1 or T_2 weighted effect. Positive MR imaging CAs are characterized for their ratios ranging from 1 to 2. On the other hand, negative MR imaging CAs have ratios higher than 10. However, if their ratio falls between 2 and 10, then the MR imaging CAs agents can provide both a T_1 and a T_2 weighted effect. [129] Table 3. presents a summary of the calculated r_1 and r_2 values at different concentrations of cDTPAA and Mn^{2+} showing that CDs-cDTPAA-Mn could be suitable to act as both a positive and a negative MR imaging CA.

Furthermore, Figure 22 illustrates the capacity of CDs-cDTPAA-Mn to enhance the contrast in MR imaging. It was noted that the use of higher concentrations of chelator does not necessarily provide a better contrast even though it allows for a greater metal ion loading onto the surface of the CDs. The reason again is related to the coordination number of Mn^{2+}. Moreover, a high number of cDTPAA ligand molecules could be interfering with the direct coordination of Mn^{2+} to protons in water hence reducing the enhancing effect. This finding is further supported by Figure 22c-e, where it was observed that the direct coordination of metals provided the highest contrast enhancement even at low concentrations of Mn^{2+}. Thus, from Figure 22 it can be stated that the functionalization of CDs with concentrations of cDTPAA as low as 83.96 μmol, and concentrations of Mn^{2+} as high as 7 wt% provided the highest contrast enhancement without sacrificing the fluorescent properties of CDs.

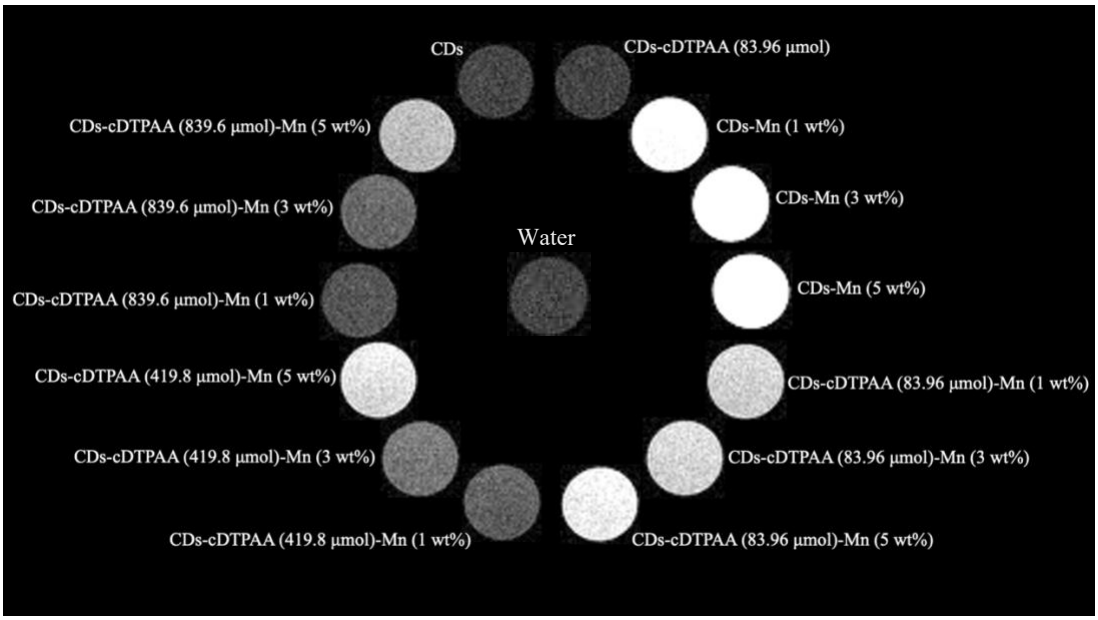

Figure 22. MR images of functionalized CDs.

3.5 Toxicity Assessment

In order to assess the potential use of Mn^{2+}-doped CDs in clinical applications, biocompatibility studies were carried out. Previous works have shown that these particular CDs have a low cytotoxicity in HeLa cells with no decrease in cell viability at concentrations up to 100 $\mu g \cdot mL^{-1}$ after 24 h.[104105] Nonetheless, a standard cell viability MST assay was performed to ensure that the CDs maintained a low cytotoxicity even after functionalization. The results evidence that after HT-29 cells have been treated with CDs for 24 h, there seems to be an increase in the proliferation, especially at high concentrations (Figure 23). This promotion of cellular growth has been observed before with negatively charged CDs, along with production of reactive oxygen species (ROS).[153,154] After CDs have been functionalized with cDTPAA and Mn^{2+}, a decrease in the viability can be observed at both the low and a high concentration of metal ions. However, this decrease is only significant for concentrations greater than 100 $\mu g \cdot mL^{-1}$ according to Student's t-test ($p<0.05$). The promotion of cell proliferation is no longer observed since the functional groups that mitigated the ferric toxicosis are being used to bind the chelator. Moreover, we compared the cytotoxicity of both nonchelated and chelated forms of Mn^{2+}. The evidence shows that Mn^{2+} decreases the cell viability to a larger extent when it is not chelated. Thus, this supports the hypothesis that the use of chelators helps reducing the cytotoxicity of metal ions in CAs. These findings suggest that CDs-cDTPAA-Mn hold a great potential to be used for biological applications with a low cytotoxicity.[155,156]

Besides low cytotoxicity, one of the requirements in the design of CAs for medical applications is that the chelating agent must strongly bind the metal ions to avoid their release into the body.[157] To investigate the stability of CDs-cDTPAA-Mn dispersions, leakage studies were carried out using NAA assessments, which revealed that approximately 1.4, 7.2, 11.2, 13.3, 13.7,

and 16.9 % of Mn^{2+} ions were released after 0.5, 1, 2, 3, 4, and 7 days, respectively (Figure 24). Despite forming thermodynamically stable complexes, cDTPAA can undergo decomplexation

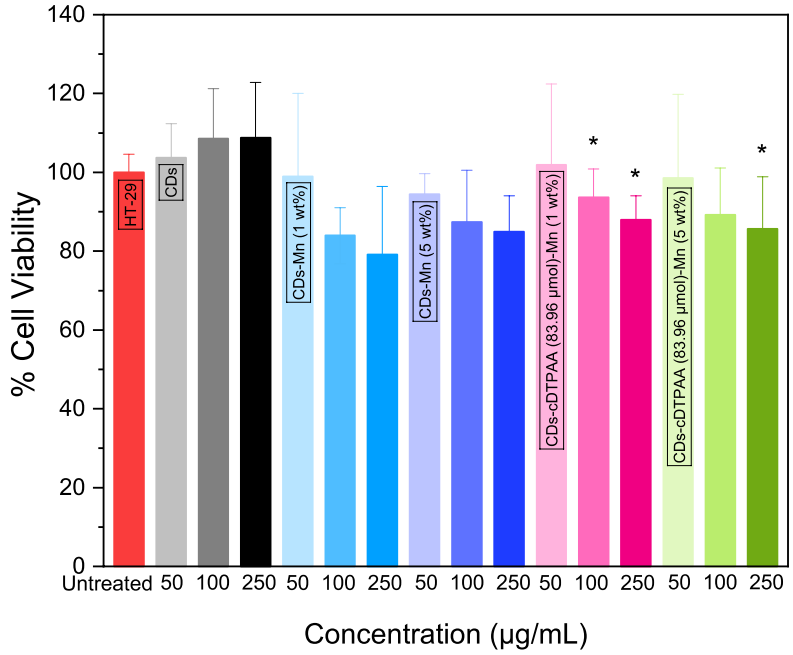

Figure 23. *In vitro* measurement of HT-29 cell viability after incubation with Mn-doped CDs at different concentrations (50,100, and 250 µg·mL^{-1}) for 24 h at 37 °C in a 5% CO_2 atmosphere. * $p<0.05$

because of a competition by available protons at pH 7.4 and this is correlated to the constant rate of dissociation. In other words, Mn^{2+} ions will compete with other protons to coordinate to cDTPAA, leading to an exchange of metal ions, also known as transmetallation, that ends in Mn^{2+} ions releasing from the structure of cDTPAA.[158,159] These findings however imply a good structural stability of CDs-cDTPAA-Mn for use in imaging applications under a conventional timescale for imaging.[129]

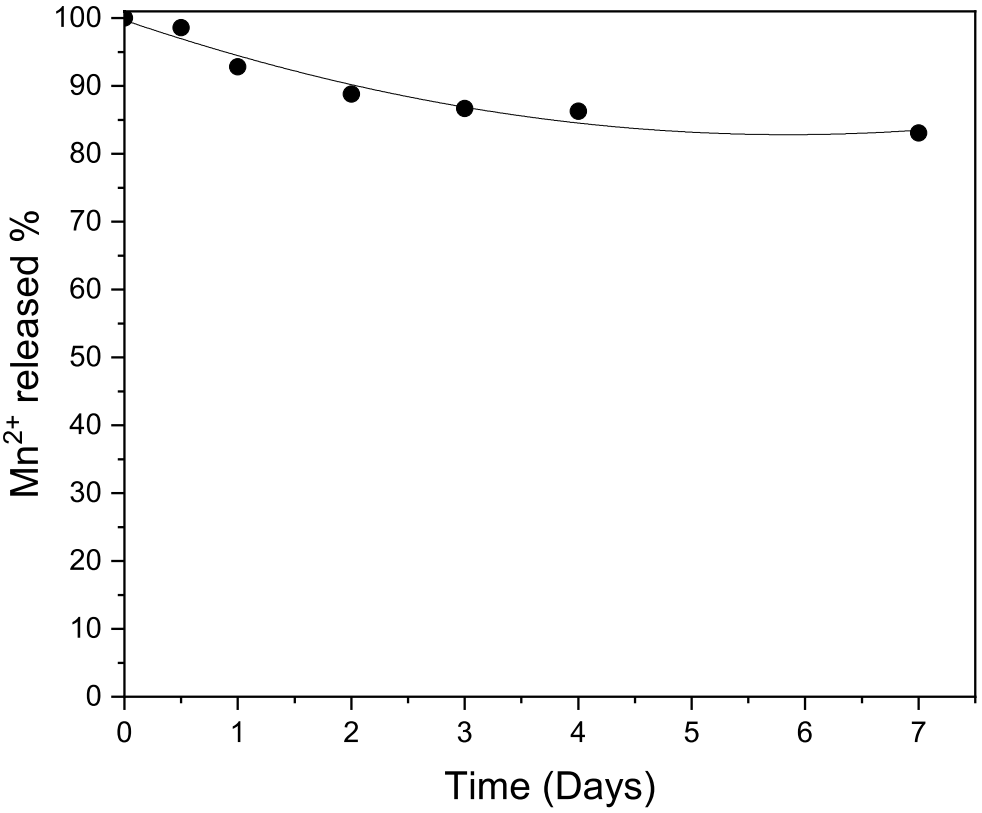

Figure 24. Percentage release of Mn^{2+} over time upon continuous dialysis of CDs-cDTPAA-Mn for 7 days.

4 Concluding Remarks

4.1 Conclusion

Fluorescent CDs were synthesized using a microwave-assisted technique involving the carbonization of L-glutathione and formamide. Characterization experiments revealed that these amorphous carbon nanoparticles have sizes of nearly 12 nm, are photostable over a prolonged light exposure period of time, display a bright dual fluorescence in the blue and red regions of the spectrum with a QY up to 5% and bear a rich surface comprising numerous functional groups including carboxyls, hydroxyls, and amines.

In this work, amine groups of the dots were used to conjugate cDTPAA, which was then able to chelate specific concentrations of paramagnetic ions, namely Mn^{2+}, to endow magnetic properties. By using a chelator, the fluorescence quenching problem that arises with the direct coordination of metal ions in the CD surface was mitigated. As a result, a nanosystem that couples fluorescence and magnetic properties was developed as a potential dual-mode FL/MR imaging contrast agent. From the optimization of the protocol to prepare the CDs-cDTPAA-Mn, it was evidenced that the optical properties of CDs are influenced following functionalization. In general, it was observed that the fluorescence emission of CDs was less intense when increasing the concentration of metal ions loaded onto their surface. Nonetheless, when the MR performance was assessed, functionalized CDs provided good contrast and relatively low r_1 and r_2 values of 0.0491 and 0.1458 $mM^{-1}\cdot s^{-1}$, respectively. From its r_1/r_2 ratio, it is evidenced that they are suitable for both T_1w images, with a minor T_2w effect.

Finally, cytotoxicity studies demonstrated that there is no significant decrease in cell viability up to a concentration of 250 $\mu g\cdot mL^{1}$, which suggests that they may have potential for

further development in clinical applications. Altogether, this water-dispersible probe that combines the superior spatial resolution of MR imaging with the high sensitivity of FL imaging, can contribute towards the development of a more efficient, safer, and more sensitive optical probe that can assist in achieving an earlier diagnosis of disease.

4.2 Future Perspectives

Mn-doped CDs chelated through cDTPAA hold a great potential as a safer multi-modal imaging probe to replace their potentially more toxic Gd-counterparts. In addition to its biocompatibility, one of the most important requirements of a good CA is its stability. If this probe were to be introduced into a biological system, the chelator, which has affinity for other metals in the body (e.g. Ca^{2+}), will un-coordinate its Mn^{2+} ions and coordinate Ca^{2+} instead. This phenomenon, also known as transmetallation, could lead to cytotoxic effects.[125] Furthermore, given the relatively low relaxivity of CDs-cDTPAA-Mn, further improvement can be made by passivating their surface with amine-rich agents (e.g. with polyethylenimine (PEIs) which has been widely used) which first, would improve their QY and second, would endow them with more chelation sites to coordinate more metal ions.[160–163] Finally, *in vivo* MR imaging, in parallel with cytotoxicity studies, will be needed to determine their applicability and viability in a "real" biological setting.[164–166]

5 References

1 A. Meyer-Baese and V. Schmid, *Pattern Recognition and Signal Analysis in Medical Imaging*, Elsevier, 2nd edn., 2014.
2 F. Kikkawa, M. Hori, S. Toyokuni and Y. Ikehara, *Plasma Medical Science*, Elsevier, 1st edn., 2018.
3 M. L. James and S. S. Gambhir, *Physiol Rev*, 2012, **92**, 897–965.
4 J. Chang, D. Schomer and T. Dragovich, *Biomed Res Int*, 2015, **2015**, 269641.
5 F. Maghsoudinia, M. B. Tavakoli, R. K. Samani, H. Motaghi, S. H. Hejazi and M. A. Mehrgardi, *J Drug Deliv Sci Technol*, 2021, **61**, 102288.
6 Y. Y. Yao, G. Gedda, W. M. Girma, C. L. Yen, Y. C. Ling and J. Y. Chang, *ACS Appl Mater Interfaces*, 2017, **9**, 13887–13899.
7 M. Zhou, L. Li, W. Xie, Z. He and J. Li, *Macromol Rapid Commun*, 2021, **42**, 2100248.
8 B. Valeur and M. N. Berberan-Santos, *J Chem Educ*, 2011, **88**, 731–738.
9 Q. Zhang, R. Wang, B. Feng, X. Zhong and K. Ostrikov, *Nat Commun*, 2021, **12**, 6856.
10 H. Zheng, Q. Wang, Y. Long, H. Zhang, X. Huang and R. Zhu, *Chemical Communications*, 2011, **47**, 10650–10652.
11 L. Gámiz-Gracia, A. M. García-Campaña, J. F. Huertas-Pérez and F. J. Lara, *Anal Chim Acta*, 2009, **640**, 7–28.
12 Y. Horowitz, R. Chen, L. Oster and I. Elyahu, *Thermoluminescence Theory and Analysis: Advances and Impact on Applications*, Elsevier, 3rd edn., 2017.
13 P. Herring and E. Widder, *Encyclopedia of Ocean Sciences*, Academic Press, 3rd edn., 2001.
14 P. Kelter, M. Mosher and A. Scott, *Chemistry: The Practical Science*, Cengage Learning, 1st edn., 2008.
15 A. Jain, C. Blu and V. Subramaniam, *Advances in Biomedical Imaging*, Elsevier, 1st edn., 2009.
16 D. Cook, *Quantum Chemistry: A Unified Approach*, Imperial College Press, London, 2nd edn., 2008.
17 R. Bansal, *Synthetic Approaches in Organic Chemistry* , Narosa Publishing House, 1st edn., 1998.
18 D. Ball, *The Basics of Spectroscopy* , SPIE-The International Society for Optical Engineering, 1sr edn., 2001.
19 F. Lenci, P. Plaza, M. Martin, N. Angelini and A. Sgarbossa, *Encyclopedia of Condensed Matter Physics*, Elsevier, 1st edn., 2005.
20 R. Yasuda, *Neurophotonics and Biomedical Spectroscopy*, Elsevier , 1st edn., 2019.
21 M. A. Omary and H. H. Patterson, *Encyclopedia of Spectroscopy and Spectrometry*, Elsevier, 1st edn., 2016.
22 C. Preston, *Nitrogen Isotope Techniques*, Academic Press, 1st edn., 1993.
23 B. Prasad, *Chemical Analysis and Material Characterization by Spectrophotometry*, Elsevier, 1st edn., 2020.
24 D. Chapman and G. Dodd, *Structure and Function of Biological Membranes*, Academic Press, 1st edn., 1971.

25 C. Zhu, J. Xin, J. Li, H. Li, X. Kang, Y. Pei and M. Zhu, *Angewandte Chemie International Edition*, 2022, **61**, 202205947.
26 A. J. Zucchero, P. L. Mcgrier and U. H. F. Bunz, *Acc Chem Res*, 2010, **43**, 397–408.
27 A. Refaat, M. L. Yap, G. Pietersz, A. P. G. Walsh, J. Zeller, B. del Rosal, X. Wang and K. Peter, *J Nanobiotechnology*, 2022, **20**, 450.
28 S. Wang, W. X. Ren, J. T. Hou, M. Won, J. An, X. Chen, J. Shu and J. S. Kim, *Chem Soc Rev*, 2021, **50**, 8887–8902.
29 J. Seo, Y. Sim, J. Kim, H. Kim, I. Cho, Y.-G. Yoon and J.-B. Chang, *bioRxiv*, 2021, 428247.
30 X. Dang, N. M. Bardhan, J. Qi, L. Gu, N. A. Eze, C. W. Lin, S. Kataria, P. T. Hammond and A. M. Belcher, *Sci Rep*, 2019, **9**, 3873.
31 M. E. Seaman, G. Contino, N. Bardeesy and K. A. Kelly, *Expert Rev Mol Med*, 2010, **12**, 20.
32 F. W. Pratiwi, C. W. Kuo, B. C. Chen and P. Chen, *Nanomedicine*, 2019, **14**, 1759–1769.
33 D. M. Chudakov, M. v. Matz, S. Lukyanov and K. A. Lukyanov, *Physiol Rev*, 2010, **90**, 1103–1163.
34 G. Hungerford, J. Benesch, J. F. Mano and R. L. Reis, *Photochemical and Photobiological Sciences*, 2007, **6**, 152–158.
35 G. Hong, A. L. Antaris and H. Dai, *Nat Biomed Eng*, 2017, **1**, 0010.
36 J. Kwon, M. S. Elgawish and S. H. Shim, *Advanced Science*, 2022, **9**, 2101817.
37 I. Gonzalez, F. Jaskolski, Y. Goldberg and M. Ashby, *Methods in Enzymology*, Elsevier, 2012, vol. 504.
38 R. Y. Kwong, M. Jerosch-Herold and B. Heydari, *Cardiovascular Magnetic Resonance Imaging*, Springer, 2nd edn., 2019.
39 V. P. B. Grover, J. M. Tognarelli, M. M. E. Crossey, I. J. Cox, S. D. Taylor-Robinson and M. J. W. McPhail, *J Clin Exp Hepatol*, 2015, **5**, 246–255.
40 R. Sadleir and A. Singh, *Electrical Properties of Tissues: Quantitative Magnetic Resonance Mapping*, Springer, 2022, vol. 1380.
41 S. C. L. Deoni, *Methods in Molecular Biology*, 2010, **711**, 65–108.
42 R. E. Hendrick, *Breast MRI*, Springer, 1st edn., 2008.
43 L. Vu, J. Morelli and J. Szklaruk, *J Hepatocell Carcinoma*, 2018, **5**, 37–50.
44 D. Pan, A. H. Schmieder, S. A. Wickline and G. M. Lanza, *Tetrahedron*, 2011, **67**, 8431–8444.
45 Z. Gao, T. Ma, E. Zhao, D. Docter, W. Yang, R. H. Stauber and M. Gao, *Small*, 2016, **12**, 556–576.
46 M. Wu and J. Shu, *Contrast Media Mol Imaging*, 2018, **2018**, 1382183.
47 M. Hori, A. Hagiwara, M. Goto, A. Wada and S. Aoki, *Invest Radiol*, 2021, **56**, 669–679.
48 P. Carretta and A. Lascialfari, *NMR-MRI, μSR and Mössbauer Spectroscopies in Molecular Magnets*, Springer, 1st edn., 2007.
49 R. A. Pooley, *Radiographics*, 2005, **25**, 1087–1099.
50 Y. Cao, L. Xu, Y. Kuang, D. Xiong and R. Pei, *J Mater Chem B*, 2017, **5**, 3431–3461.
51 L. M. de Leõn-Rodríguez, A. F. Martins, M. C. Pinho, N. M. Rofsky and A. D. Sherry, *Journal of Magnetic Resonance Imaging*, 2015, **42**, 545–565.

52 A. S. Thakor, J. v. Jokerst, P. Ghanouni, J. L. Campbell, E. Mittra and S. S. Gambhir, *Journal of Nuclear Medicine*, 2016, **57**, 1833–1837.
53 Y. D. Xiao, R. Paudel, J. Liu, C. Ma, Z. S. Zhang and S. K. Zhou, *Int J Mol Med*, 2016, **38**, 1319–1326.
54 C. Do, J. DeAguero, A. Brearley, X. Trejo, T. Howard, G. P. Escobar and B. Wagner, *Kidney360*, 2020, **1**, 561–568.
55 L. Leone, G. Ferrauto, M. Cossi, M. Botta and L. Tei, *Front Chem*.
56 U.S. Food and Drug Administration, *FDA warns that gadolinium-based contrast agents (GBCAs) are retained in the body; requires new class warnings*, 2017.
57 M. Mathur, J. R. Jones and J. C. Weinreb, *Radiographics*, 2020, **40**, 153–162.
58 N. S. el Saghir, I. I. Elhajj, F. B. Geara and M. H. Hourani, *BMC Cancer*, 2005, **5**, 94.
59 V. Jacques, S. Dumas, W.-C. Sun, J. S. Troughton, M. T. Greenfield and P. Caravan, *Invest Radiol*, 2010, **45**, 613–624.
60 Y. Li, H. Dong, Q. Tao, C. Ye, M. Yu, J. Li, H. Zhou, S. Yang, G. Ding and X. Xie, *Biomaterials*, 2020, **250**, 120056.
61 J. Xiao, X. M. Tian, C. Yang, P. Liu, N. Q. Luo, Y. Liang, H. B. Li, D. H. Chen, C. X. Wang, L. Li and G. W. Yang, *Sci Rep*, 2013, **3**, 3424.
62 L. Yan, Y. Yang, C. Q. Ma, X. Liu, H. Wang and B. Xu, *Carbon N Y*, 2016, **109**, 598–607.
63 P. Zhao, X. Li, G. Baryshnikov, B. Wu, H. Ågren, J. Zhang and L. Zhu, *Chem Sci*, 2018, **9**, 1323–1329.
64 J. Y. Li, Y. Liu, Q. W. Shu, J. M. Liang, F. Zhang, X. P. Chen, X. Y. Deng, M. T. Swihart and K. J. Tan, *Langmuir*, 2017, **33**, 1043–1050.
65 J. Othong, J. Boonmak, V. Promarak, F. Kielar and S. Youngme, *ACS Appl Mater Interfaces*, 2019, **11**, 44421–44429.
66 W. Kwon and S. W. Rhee, *Chemical Communications*, 2012, **48**, 5256–5258.
67 M. Serhan, M. Sprowls, D. Jackemeyer, M. Long, I. D. Perez, W. Maret, N. Tao and E. Forzani, in *AIChE Annual Meeting, Conference Proceedings*, American Institute of Chemical Engineers, 2019, vol. 2019- November.
68 L. Ge, G. Hu, B. Shi, Q. Guo, L. Li, L. Zhao and J. Li, *Appl Phys A Mater Sci Process*, 2019, **125**, 641.
69 A. Kaczmarek, J. Hoffman, J. Morgiel, T. M. Mo´scicki, L. Stobí Nski, Z. Szymá Nski and A. Małolepszy, *Materials*, 2021, **14**, 1–13.
70 F. J. Chao-Mujica, L. Garcia-Hernández, S. Camacho-López, M. Camacho-López, M. A. Camacho-López, D. Reyes Contreras, A. Pérez-Rodríguez, J. P. Peña-Caravaca, A. Páez-Rodríguez, J. G. Darias-Gonzalez, L. Hernandez-Tabares, O. Arias de Fuentes, E. Prokhorov, N. Torres-Figueredo, E. Reguera and L. F. Desdin-García, *J Appl Phys*, 2021, **129**, 163301.
71 X. Hong, L. He, X. Ma, W. Yang, Y. Chen, L. Zhang, H. Yan, Z. Li and L. Mai, *Nano Res*, 2017, **10**, 3743–3753.
72 L. A. Kolahalam, I. v. Kasi Viswanath, B. S. Diwakar, B. Govindh, V. Reddy and Y. L. N. Murthy, *Mater Today Proc*, 2019, **18**, 2182–2190.
73 G. N. Kokila, C. Mallikarjunaswamy and V. L. Ranganatha, *Inorganic and Nano-Metal Chemistry*, 2022, 1–30.

74 J. Jeevanandam, A. Barhoum, Y. S. Chan, A. Dufresne and M. K. Danquah, *Beilstein Journal of Nanotechnology*, 2018, **9**, 1050–1074.
75 V. Harish, D. Tewari, M. Gaur, A. B. Yadav, S. Swaroop, M. Bechelany and A. Barhoum, *Nanomaterials*, 2022, **12**, 457.
76 N. Baig, I. Kammakakam, W. Falath and I. Kammakakam, *Mater Adv*, 2021, **2**, 1821–1871.
77 N. Chanda, R. Shukla, K. v. Katti and R. Kannan, *Nano Lett*, 2009, **9**, 1798–1805.
78 P. Si, N. Razmi, O. Nur, S. Solanki, C. M. Pandey, R. K. Gupta, B. D. Malhotra, M. Willander and A. de La Zerda, *Nanoscale Adv*, 2021, **3**, 2679–2698.
79 J. G. Rho, H. S. Han, J. H. Han, H. Lee, V. Q. Nguyen, W. H. Lee, S. Kwon, S. Heo, J. Yoon, H. H. Shin, E. young Lee, H. Kang, S. Yang, E. K. Lee, J. H. Park and W. Kim, *Journal of Controlled Release*, 2018, **279**, 89–98.
80 J. Qi, Y. Fang, R. T. K. Kwok, X. Zhang, X. Hu, J. W. Y. Lam, D. Ding and B. Z. Tang, *ACS Nano*, 2017, **11**, 7177–7188.
81 T. Briolay, T. Petithomme, M. Fouet, N. Nguyen-Pham, C. Blanquart and N. Boisgerault, *Mol Cancer*, 2021, **20**, 55.
82 R. B. Onyancha, K. E. Ukhurebor, U. O. Aigbe, O. A. Osibote, H. S. Kusuma and H. Darmokoesoemo, *Adsorption Science and Technology*, 2022, **2022**, 4438286.
83 A. G. Crevillen, A. Escarpa and C. D. Garcia, *Carbon-based Nanomaterials in Analytical Chemistry*, Royal Society of Chemistry, 1st edn., 2018.
84 K. D. Patel, R. K. Singh and H. W. Kim, *Mater Horiz*, 2019, **6**, 434–469.
85 N. Kumar and S. Kumbhat, *Essentials in Nanoscience and Nanotechnology*, John Wiley & Sons, Inc., 1st edn., 2016.
86 X. Xu, R. Ray, Y. Gu, H. J. Ploehn, L. Gearheart, K. Raker and W. A. Scrivens, *J Am Chem Soc*, 2004, **126**, 12736–12737.
87 J. Liu, R. Li and B. Yang, *ACS Cent Sci*, 2020, **6**, 2179–2195.
88 M. L. Liu, B. bin Chen, C. M. Li and C. Z. Huang, *Green Chemistry*, 2019, **21**, 449–471.
89 Q. Guan, R. Su, M. Zhang, R. Zhang, W. Li, D. Wang, M. Xu, L. Fei and Q. Xu, *New Journal of Chemistry*, 2019, **43**, 3050–3058.
90 C. Kang, Y. Huang, H. Yang, X. F. Yan and Z. P. Chen, *Nanomaterials*, 2020, **10**, 1–24.
91 L. Đorđević, F. Arcudi and M. Prato, *Nat Protoc*, 2019, **14**, 2931–2953.
92 A. Sciortino, A. Cannizzo and F. Messina, *C (Basel)*, 2018, **4**, 67.
93 Y. Park, J. Yoo, B. Lim, W. Kwon and S. W. Rhee, *J Mater Chem A Mater*, 2016, **4**, 11582–11603.
94 T. v. de Medeiros, J. Manioudakis, F. Noun, J. R. Macairan, F. Victoria and R. Naccache, *J Mater Chem C Mater*, 2019, **7**, 7175–7195.
95 L. M. T. Phan and S. Cho, *Bioinorg Chem Appl*, 2022, **2022**, 9303703.
96 S. Das, L. Ngashangva and P. Goswami, *Micromachines (Basel)*, 2021, **12**, 1–36.
97 L. Cui, X. Ren, M. Sun, H. Liu and L. Xia, *Nanomaterials*, 2021, **11**, 3419.
98 Q. Zhao, W. Song, B. Zhao and B. Yang, *Mater Chem Front*, 2020, **4**, 472–488.
99 P. Koutsogiannis, E. Thomou, H. Stamatis, D. Gournis and P. Rudolf, *Adv Phys X*, 2020, **5**, 1758592.
100 X. Wang, Y. Feng, P. Dong and J. Huang, *Front Chem*, 2019, **7**, 671.

101 J. R. Macairan, T. v. de Medeiros, M. Gazzetto, F. Yarur Villanueva, A. Cannizzo and R. Naccache, *J Colloid Interface Sci*, 2022, **606**, 67–76.
102 M. Liu, *Nanoarchitectonics*, 2020, **1**, 1–12.
103 F. Noun, E. A. Jury and R. Naccache, *Sensors (Switzerland)*, 2021, **21**, 1–13.
104 J. R. Macairan, I. Zhang, A. Clermont-Paquette, R. Naccache and D. Maysinger, *Particle and Particle Systems Characterization*, 2020, **37**, 1900430.
105 J. R. Macairan, D. B. Jaunky, A. Piekny and R. Naccache, *Nanoscale Adv*, 2019, **1**, 105–113.
106 Y. Wang and A. Hu, *J Mater Chem C Mater*, 2014, **2**, 6921–6939.
107 P. Lesani, A. H. Mohamad Hadi, Z. Lu, S. Palomba, E. J. New and H. Zreiqat, *Commun Mater*, 2021, **2**, 108.
108 J. Wang and J. Qiu, *J Mater Sci*, 2016, **51**, 4728–4738.
109 I. Perelshtein, N. Perkas, S. Rahimipour and A. Gedanken, *Nanomaterials*, 2020, **10**, 1–8.
110 C. L. Shen, H. R. Liu, Q. Lou, F. Wang, K. K. Liu, L. Dong and C. X. Shan, *Theranostics*, 2022, **12**, 2860–2893.
111 V. Naik, P. Zantye, D. Gunjal, A. Gore, P. Anbhule, M. Kowshik, S. v. Bhosale and G. Kolekar, *ACS Appl Bio Mater*, 2019, **2**, 2069–2077.
112 X. Geng, Y. Sun, Z. Li, R. Yang, Y. Zhao, Y. Guo, J. Xu, F. Li, Y. Wang, S. Lu and L. Qu, *Small*, 2019, **15**, 1901517.
113 Y. F. Wu, H. C. Wu, C. H. Kuan, C. J. Lin, L. W. Wang, C. W. Chang and T. W. Wang, *Sci Rep*, 2016, **6**, 21170.
114 Y. Jiao, Y. Gao, Y. Meng, W. Lu, Y. Liu, H. Han, S. Shuang, L. Li and C. Dong, *ACS Appl Mater Interfaces*, 2019, **11**, 16822–16829.
115 X. W. Hua, Y. W. Bao, J. Zeng and F. G. Wu, *ACS Appl Mater Interfaces*, 2019, **11**, 32647–32658.
116 M. Zhang, R. Su, J. Zhong, L. Fei, W. Cai, Q. Guan, W. Li, N. Li, Y. Chen, L. Cai and Q. Xu, *Nano Res*, 2019, **12**, 815–821.
117 R. Foulkes, E. Man, J. Thind, S. Yeung, A. Joy and C. Hoskins, *Biomater Sci*, 2020, **8**, 4653–4664.
118 A. Kaur, E. J. New and M. Sunde, *ACS Sens*, 2020, **5**, 2268–2282.
119 S. Zhou, B. Zhang, E. Sturm, D. L. Teagarden, C. Schöneich, P. Kolhe, L. M. Lewis, B. K. Muralidhara and S. K. Singh, *J Pharm Sci*, 2010, **99**, 4239–4250.
120 Thermo Scientific, *Crosslinking Technical Handbook*, n.d.
121 Y. Shi, Y. Pan, J. Zhong, J. Yang, J. Zheng, J. Cheng, R. Song and C. Yi, *Carbon N Y*, 2015, **93**, 742–750.
122 S. Zheng, N. Yu, C. Han, T. Xie, B. Dou, Y. Kong, F. Zuo, M. Shi and K. Xu, *Biochem Biophys Res Commun*, 2019, **511**, 207–213.
123 S. H. Chiu, G. Gedda, W. M. Girma, J. K. Chen, Y. C. Ling, A. v. Ghule, K. L. Ou and J. Y. Chang, *Acta Biomater*, 2016, **46**, 151–164.
124 N. Gong, H. Wang, S. Li, Y. Deng, X. Chen, L. Ye and W. Gu, *Langmuir*, 2014, **30**, 10933–10939.
125 D. Pan, A. H. Schmieder, S. A. Wickline and G. M. Lanza, *Tetrahedron*, 2011, **67**, 8431–8444.
126 Z. Ji, P. Ai, C. Shao, T. Wang, C. Yan, L. Ye and W. Gu, *ACS Biomater Sci Eng*, 2018, **4**, 2089–2094.

127 N. Irmania, K. Dehvari, G. Gedda, P. J. Tseng and J. Y. Chang, *J Biomed Mater Res B Appl Biomater*, 2020, **108**, 1616–1625.
128 S. A. Rub Pakkath, S. S. Chetty, P. Selvarasu, A. Vadivel Murugan, Y. Kumar, L. Periyasamy, M. Santhakumar, S. R. Sadras and K. Santhakumar, *ACS Biomater Sci Eng*, 2018, **4**, 2581–2596.
129 J. S. Lin, Y. W. Tsai, K. Dehvari, C. C. Huang and J. Y. Chang, *Nanoscale*, 2019, **11**, 20917–20931.
130 L. Yue, H. Li, Q. Liu, D. Guo, J. Chen, Q. Sun, Y. Xu and F. Wu, *Microchimica Acta*, 2019, **186**, 315.
131 S. Sun, L. Zhao, D. Wu, H. Zhang, H. Lian, X. Zhao, A. Wu and L. Zeng, *ACS Appl Bio Mater*, 2021, **4**, 1969–1975.
132 S. Caspani, R. Magalhães, J. P. Araújo and C. T. Sousa, *Materials*, 2020, **13**, 2586.
133 J. R. Macairan, I. Zhang, A. Clermont-Paquette, R. Naccache and D. Maysinger, *Particle and Particle Systems Characterization*, 2020, **37**, 1900430.
134 J. R. Macairan, D. B. Jaunky, A. Piekny and R. Naccache, *Nanoscale Adv*, 2019, **1**, 105–113.
135 C. H. Paik, M. A. Ebbert, P. R. Murphy, C. R. Lassman, R. C. Reba, W. C. Eckelman, K. Y. Pak, J. Powe, Z. Steplewski and H. Koprowski, *J Nucl Med*, 1983, **24**, 1158–1163.
136 R. R. Greenberg, P. Bode and E. A. de Nadai Fernandes, *Spectrochim Acta Part B At Spectrosc*, 2011, **66**, 193–241.
137 M. V. Frontasyeva, *Physics of Particles and Nuclei*, 2011, **42**, 332–378.
138 T. V. de Medeiros, J. Manioudakis, F. Noun, J. R. Macairan, F. Victoria and R. Naccache, *J Mater Chem C Mater*, 2019, **7**, 7175–7195.
139 Y. Liu, N. Xiao, N. Gong, H. Wang, X. Shi, W. Gu and L. Ye, *Carbon N Y*, 2014, **68**, 258–264.
140 A. Pal, M. P. Sk and A. Chattopadhyay, *Mater Adv*, 2020, **1**, 525–553.
141 Y. Chen and T. C. Bond, *Atmos. Chem. Phys*, 2010, **10**, 1773–1787.
142 F. Noun, E. A. Jury and R. Naccache, *Sensors (Switzerland)*, 2021, **21**, 1–13.
143 N. Niu, Z. Ma, F. He, S. Li, J. Li, S.-X. Liu and P. Yang, *Langmuir*, 2017, **33**, 5786–5795.
144 M. Lan, S. Zhao, Z. Zhang, L. Yan, L. Guo, G. Niu, J. Zhang, J. Zhao, H. Zhang, P. Wang, G. Zhu, C. S. Lee and W. Zhang, *Nano Res*, 2017, **10**, 3113–3123.
145 Q. Wang, Z. Feng, H. He, X. Hu, J. Mao, X. Chen, L. Liu, X. Wei, D. Liu, S. Bi, X. Wang, B. Ge, D. Yu and F. Huang, *Chemical Communications*, 2021, **57**, 5554–5557.
146 H. Szmacinski and J. R. Lakowicz, *Sensors and Actuators B*, 1995, **29**, 16–24.
147 Y. Xie, M. C. Arno, J. T. Husband, M. Torrent-Sucarrat and R. K. O'Reilly, *Nat Commun*, 2020, **11**, 2460.
148 F. Zu, F. Yan, Z. Bai, J. Xu, Y. Wang, Y. Huang and X. Zhou, *Microchimica Acta*, 2017, **184**, 1899–1914.
149 P. Yu, X. Wen, Y. R. Toh and J. Tang, *Journal of Physical Chemistry C*, 2012, **116**, 25552–25557.
150 A. v. Longo, A. Sciortino, M. Cannas and F. Messina, *Physical Chemistry Chemical Physics*, 2020, **22**, 13398–13407.
151 C. Liu, F. Zhang, J. Hu, W. Gao and M. Zhang, *Front Chem*, 2021, **8**, 605028.

152 N. Irmania, K. Dehvari, G. Gedda, P. J. Tseng and J. Y. Chang, *J Biomed Mater Res B Appl Biomater*, 2020, **108**, 1616–1625.
153 M. Havrdova, K. Hola, J. Skopalik, K. Tomankova, M. Petr, K. Cepe, K. Polakova, J. Tucek, A. B. Bourlinos and R. Zboril, *Carbon N Y*, 2016, **99**, 238–248.
154 G. Getachew, C. Korupalli, A. Rasal and J. Chang, *Compos B Eng*, 2021, **226**, 109364.
155 Z. Gao, G. Shen, X. Zhao, N. Dong, P. Jia, J. Wu, D. Cui, Y. Zhang and Y. Wang, *Nanoscale Res Lett*, 2013, **8**, 1–8.
156 S. Şimşek, A. A. Şüküroğlu, D. Yetkin, B. Özbek, D. Battal and R. Genç, *Sci Rep*, 2020, **10**, 13880.
157 M. Y. Berezin, *Nanotechnology for Biomedical Imaging and Diagnostics*, John Wiley & Sons, Inc., 1st edn., 2015.
158 F. Knoepp, J. Bettmer and M. Fronius, *Biochim Biophys Acta Biomembr*, 2017, **1859**, 1040–1048.
159 J. M. Idée, M. Port, I. Raynal, M. Schaefer, S. le Greneur and C. Corot, *Fundam Clin Pharmacol*, 2006, **20**, 563–576.
160 Y. Hailing, L. Xiufang, W. Lili, L. Baoqiang, H. Kaichen, H. Yongquan, Z. Qianqian, M. Chaoming, R. Xiaoshuai, Z. Rui, L. Hui, P. Pengfei and S. Hong, *Nanoscale*, 2020, **12**, 17222–17237.
161 Q. Liu, Z. Dong, A. Hao, X. Guo and W. Dong, *Talanta*, 2021, **221**, 121372.
162 Y. Bai, B. Zhang, L. Chen, Z. Lin, X. Zhang, D. Ge, W. Shi and Y. Sun, *Nanoscale Res Lett*, 2018, **13**, 287.
163 R. Mohammadinejad, A. Dadashzadeh, S. Moghassemi, M. Ashrafizadeh, A. Dehshahri, A. Pardakhty, H. Sassan, S. M. Sohrevardi and A. Mandegary, *J Adv Res*, 2019, **18**, 81–93.
164 Y. Zhao, X. Hao, W. Lu, R. Wang, X. Shan, Q. Chen, G. Sun and J. Liu, *ACS Appl Nano Mater*, 2018, **1**, 2544–2551.
165 N. Liu, Y. Shi, J. Guo, H. Li, Q. Wang, M. Song, Z. Shi, L. He, X. Su, J. Xie and X. Sun, *Nano Res*, 2019, **12**, 3037–3043.
166 D. Choi, S. Jeon, D. G. You, W. Um, J. Y. Kim, H. Y. Yoon, H. Chang, D. E. Kim, J. H. Park, H. Kim and K. Kim, *Nanotheranostics*, 2018, **2**, 117–127.